Supplementary Information for

Single-fiber hyperspectral imaging via nanophotonic disordered dispersion

Yuchen Ma[1,2], Jiachen Wu[1], Chang-Yin Ji[2], Liangcai Cao[1*], Guangwei Hu[2*]

[1]State Key Laboratory of Precision Measurement Technology and Instruments, Department of Precision Instrument, Tsinghua University, Beijing, 100084, China.

[2]School of Electrical and Electronic Engineering, Nanyang Technological University, Singapore, 639798, Singapore.

*Corresponding author(s). E-mail(s): clc@tsinghua.edu.cn; guangwei.hu@ntu.edu.sg;

Contents

1 Comparison between conventional imaging schemes and our strategy

Compared to conventional imaging schemes, our approach offers both a high-dimensional detection capacity and a compact form factor (Fig. S1 and Fig. 1d), thanks to the dispersion-space encoding and compressive mapping capability enabled by disordered dispersion.

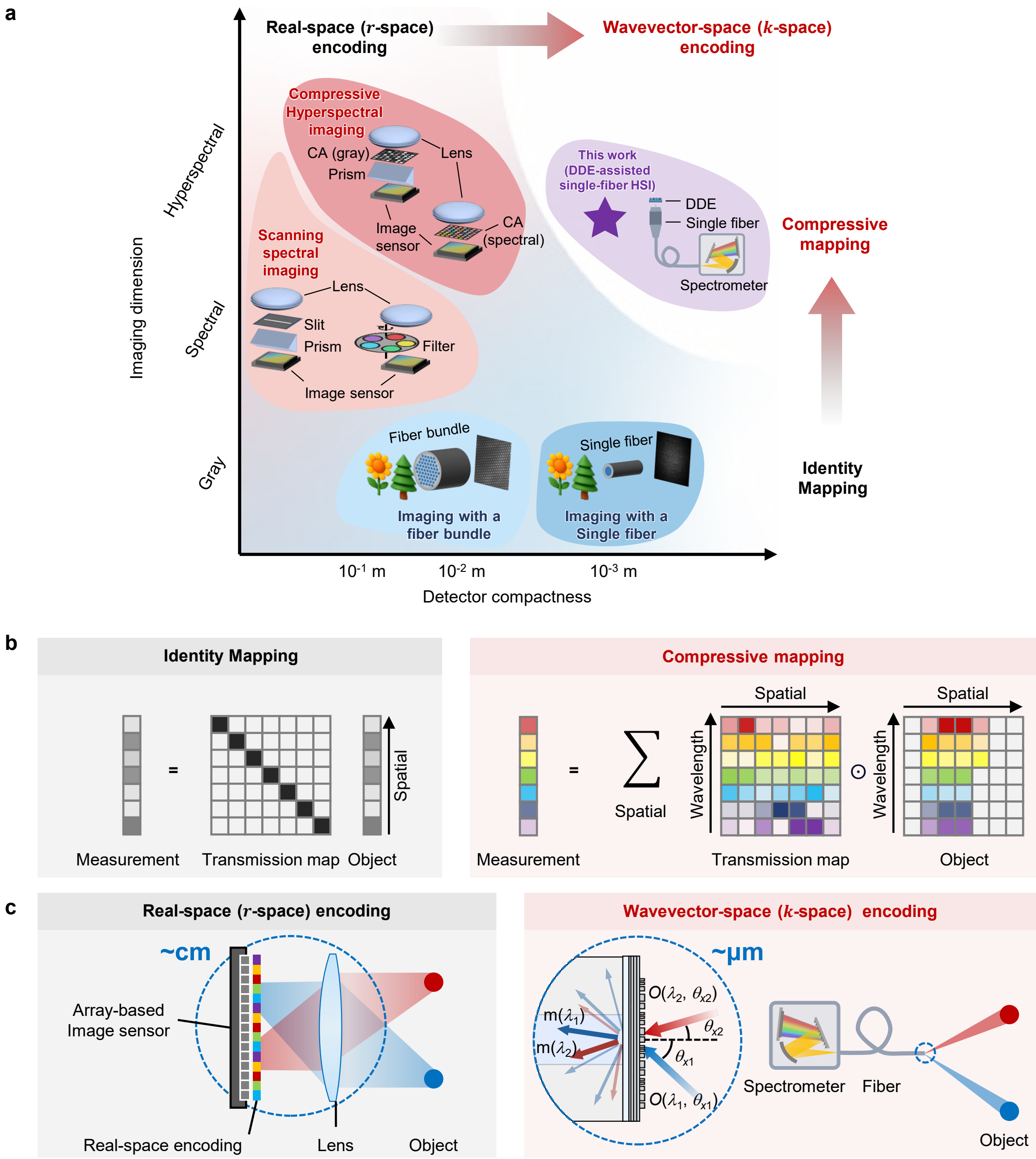

Fig. S1: **Comparison between conventional imaging schemes and our strategy.** From the perspective of encoding strategies, our method constructs a disordered transmission map that compressively encodes high-dimensional spectral-angular signals into 1D spectral measurements, thereby enabling higher-dimensional detection. From the perspective of physical implementation, our method achieves wavevector-space encoding instead of real-space encoding, compressing the imager's footprint to the single-pixel level, comparable to the size of a single optical fiber's aperture.

From the perspective of enhancing imaging dimensionality, conventional fiber-based imaging strategies offer ultra-compact probes but face inherent limitations in achieving high-dimensional detection. In fiber bundle systems, each fiber transmits a single image pixel, and the overall imaging throughput is fundamentally constrained by the core density [1–7]. Multimode fibers (MMFs), on the other hand, support a significantly higher number of spatial modes, enabling high-resolution coherent light control and acquisition [8–14]. However, the extreme sensitivity of the transmission matrix to perturbations makes high-dimensional spectral imaging with MMFs nearly infeasible. Spectral encoding techniques [15–19] attempt to address this by inferring spatial information from spectral measurements. Nevertheless, these methods rely on the assumption that the object possesses a broadband, known, and spatially uniform spectral distribution. This assumption breaks down when the object's spectral properties vary across spatial locations.

The common limitation among the above strategies lies in their reliance on an identity mapping between the object and the measurement domain, corresponding to a diagonal transmission matrix. In such frameworks, the optical field must be acquired, transmitted, and reconstructed with minimal distortion. Consequently, the limited transmission capacity of a single fiber cannot accommodate high-dimensional imaging.

In contrast, our framework establishes a compressive mapping between 2D spectral-angular objects and 1D spectral-only measurements. Our disordered-dispersion encoder generates an encoding function that aligns with compressive sensing theory (corresponding to a transmission matrix with a disordered distribution). This architecture breaks the constraints of direct mapping and enables high-dimensional detection within the limited channel capacity of a single fiber, as illustrated in Fig. S1a and S1b.

From the perspective of device form factor reduction, hyperspectral imaging technologies have progressively reduced the size of imaging components. Traditional hyperspectral systems rely on scanning techniques involving slits and prisms or tunable filters, capturing a slice of the hyperspectral data cube in a single shot. Spatial or spectral scanning is then used to reconstruct the full data cube [20,21]. With the advancement of computational techniques, coded aperture snapshot spectral imaging (CASSI) was developed to encode the hyperspectral cube before capturing it through intensity-only measurements, which is a compressive process [22–25]. CASSI not only increases the number of spectral channels captured in a single shot but also eliminates mechanical scanning, thereby enhancing system integration. Recent advances in micro/nanofabrication have enabled on-chip implementations of spectral coding components, replacing conventional CASSI elements with compact integrated devices [26–30].

These devices consolidate the coding and dispersion functions into a single planar structure, reducing the system size to the centimeter scale. This evolution clearly indicates that the physical size of the encoding device directly determines the overall footprint of the hyperspectral imaging system.

Despite these advances, further miniaturization of the spectral encoding stage—down to micrometer scales compatible with fiber-based platforms—remains a significant challenge. Traditional hyperspectral encoders introduce real-space inhomogeneity using elements like coded apertures or filters, coupled with pixelated image sensors (CCD or CMOS). These systems require relatively large apertures (on the order of centimeters) to maintain sufficient encoding and detection throughput. When such designs are scaled down to match fiber apertures, the number of available encoding channels drops drastically.

Our method circumvents this bottleneck by eliminating real-space inhomogeneity. Instead, we engineer wavevector-space inhomogeneity through tailored dispersion characteristics at the optical interface. This strategy allows for high-throughput encoding and recording within a single-pixel aperture, making it feasible to perform high-dimensional imaging with single-fiber probes, as illustrated in Fig. S1a and S1c.

We further compare our prototype with recent nanophotonics-assisted coded-aperture hyperspectral imaging systems. The main advantage of our method is its compact encoding aperture. Representative systems typically require millimeter-scale encoding apertures, such as 2.10 mm $\times$ 2.10 mm in Ref.[26], 7.74 mm $\times$ 6.33 mm in Ref.[27], 10.56 mm $\times$ 5.94 mm in Ref.[29], and 7.07 mm $\times$ 7.07 mm for V1 or 5.12 mm $\times$ 5.12 mm for V2 in Ref.[30]. In comparison, the active aperture of our DDE is only 0.15 mm $\times$ 0.15 mm, corresponding to a reduction of approximately 2.3–3.4 orders of magnitude in encoding area.

The spectral coverage of our system is 400–700 nm, comparable to these visible-range hyperspectral imaging demonstrations. When angular reconstruction is not considered and the incident angular distribution is fixed, the wavelength sampling/resolution is limited by the spectrometer used in the experiment, which is 0.8 nm. This is comparable to the reported spectral resolutions of 1 nm in Ref.[26] and 0.8 nm in Ref.[27].

Compared with large-aperture nanophotonic hyperspectral imagers, our system has a lower spatial/angular resolution and fewer spatial/angular channels. Therefore, the present work does not aim to outperform these systems in spatial resolution, but instead demonstrates a different miniaturization route: wavevector-space disordered-dispersion encoding enables hyperspectral imaging within a fiber-compatible aperture.

2 Mechanism and design strategy of disordered dispersion

In this section, we present the mechanism and design of disordered dispersion using meta-optical structures. The overall strategy, as illustrated in Fig. S2, consists of three key steps: (I) introducing mode diversity, (II) enhancing mode density, and (III) inducing coupling between these multiple modes.

Mode diversity ensures that the output field exhibits varied distributions, which is crucial for generating diverse responses across different angles and wavelengths. To achieve this diversity over a wide range of incident angles and wavelengths, we broaden the wavevector and frequency ranges covered by these modes, a process that corresponds to enhancing mode density. Furthermore, inducing mode coupling amplifies their high-density and diverse characteristics. Using this approach, we develop the disordered-dispersion encoder featuring compact, periodic structures in real space. However, in momentum space, the high mode density and diverse modal properties enable distinct spectral-angular responses.

2.1 Introducing mode diversity

To introduce mode diversity, we employ two distinct structures: gratings and thin-film structures. Periodic gratings and periodic thin films (1D photonic crystals) provide periodic dielectric constant distributions in the x and z directions, respectively, yielding diverse modes with distinct band structure shapes.

Consider a simple grating with a period of 0.5 µm, consisting of 250 nm grooves and ridges with a height of 500 nm, made from silicon nitride on a quartz substrate. The transmission map of the 0th order diffraction of s polarized light, shown in Fig. S2a, reveals a continuous and linear band structure across the (f, k_x) plane. The rigorous coupled wave analysis (RCWA) method[31] is used to compute the diffraction. We next examine a periodic thin film consisting of alternating 100 nm thick layers of silicon nitride and silicon dioxide. The transmission is computed using the transfer matrix method (TMM)[32]. Figure S2b presents the transmission map for s-polarized light, revealing a bandgap that suppresses transmission between approximately 440 and 500 terahertz.

Notably, while periodic gratings and thin films offer mode diversity, this diversity remains relatively simple, as evidenced by their straightforward band structures or confinement to specific regions in the wavevector-frequency plane due to band gaps. These limitations are addressed in the next section by enhancing mode density.

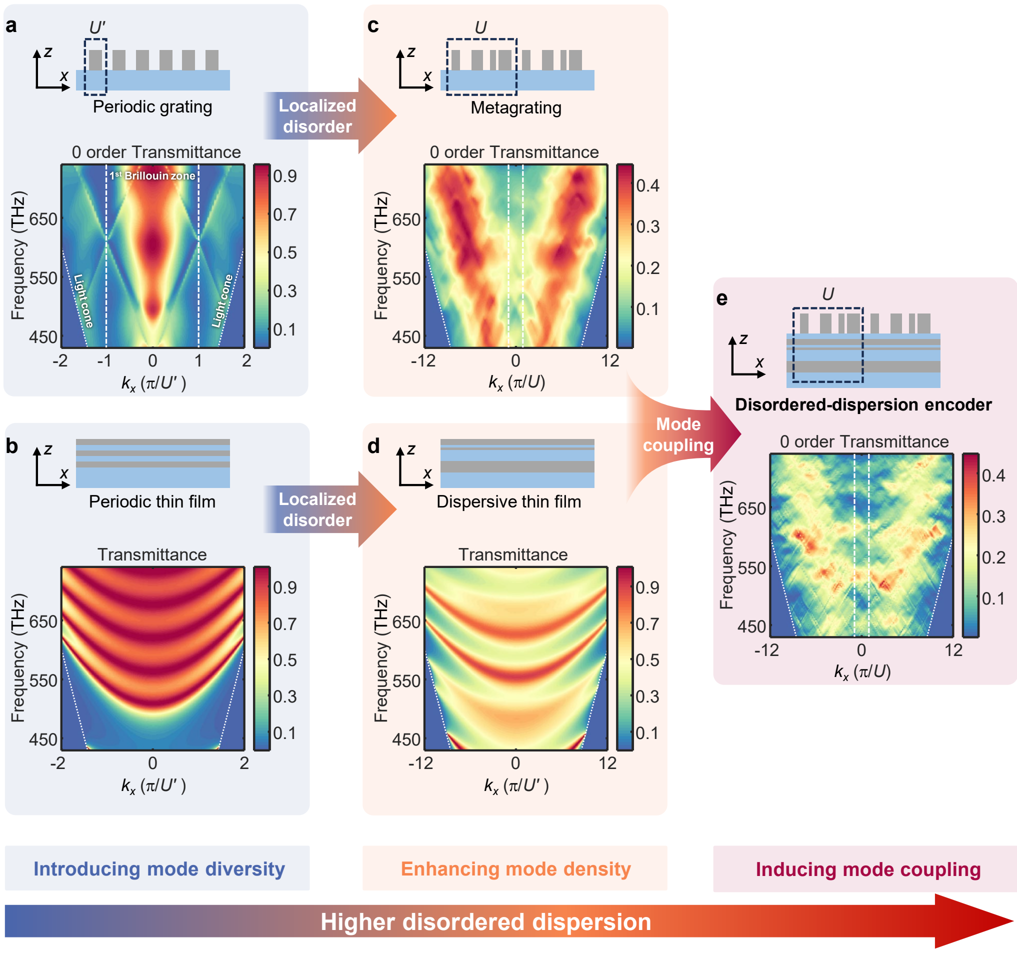

Fig. S2: **Mechanism of generating disordered dispersion. a** and **b**, We harness two different structures to introduce mode diversity. **c**, Introducing localized disorder to form superlattices creates a metagrating, which leads to band folding and increased mode diversity, corresponding to more diffraction orders and greater variation in diffracted intensity. **d**, By designing the layer thickness of the thin film, the dispersive properties can be tailored. **e**, The coupling between the metagrating and the dispersive thin film provides highly dense and diverse eigenmodes across the frequency-wavevector domain.

2.2 Enhancing mode density

To increase mode density, we introduce localized disorder into these structures. For the grating, this disorder is modeled as a metagrating with periodic superlattices and asymmetric arrangements, transforming the band diagram (Fig. S2a) into zone-folded versions (Fig. S2c), yielding more intricate band structures with features like splitting and crossing. Similarly, disrupting the periodic arrangement of the thin film reshapes its band structure, eliminating the band gap and enabling dispersion over a broader frequency range. These changes produce a diverse set of excitable modes, enhancing modal richness.

To achieve optimal performance, we deliberately design the parameters of these disordered structures, as depicted in Fig. S3. In the metagrating's superlattice of $U = 3$ μm, each of the G sub-gratings is defined by the widths of the background (air) and dielectric (silicon nitride), denoted as $(l_1, l_2, \ldots, l_G; w_1, w_2, \ldots, w_G)$ (Fig. S3a). This design aims to achieve a

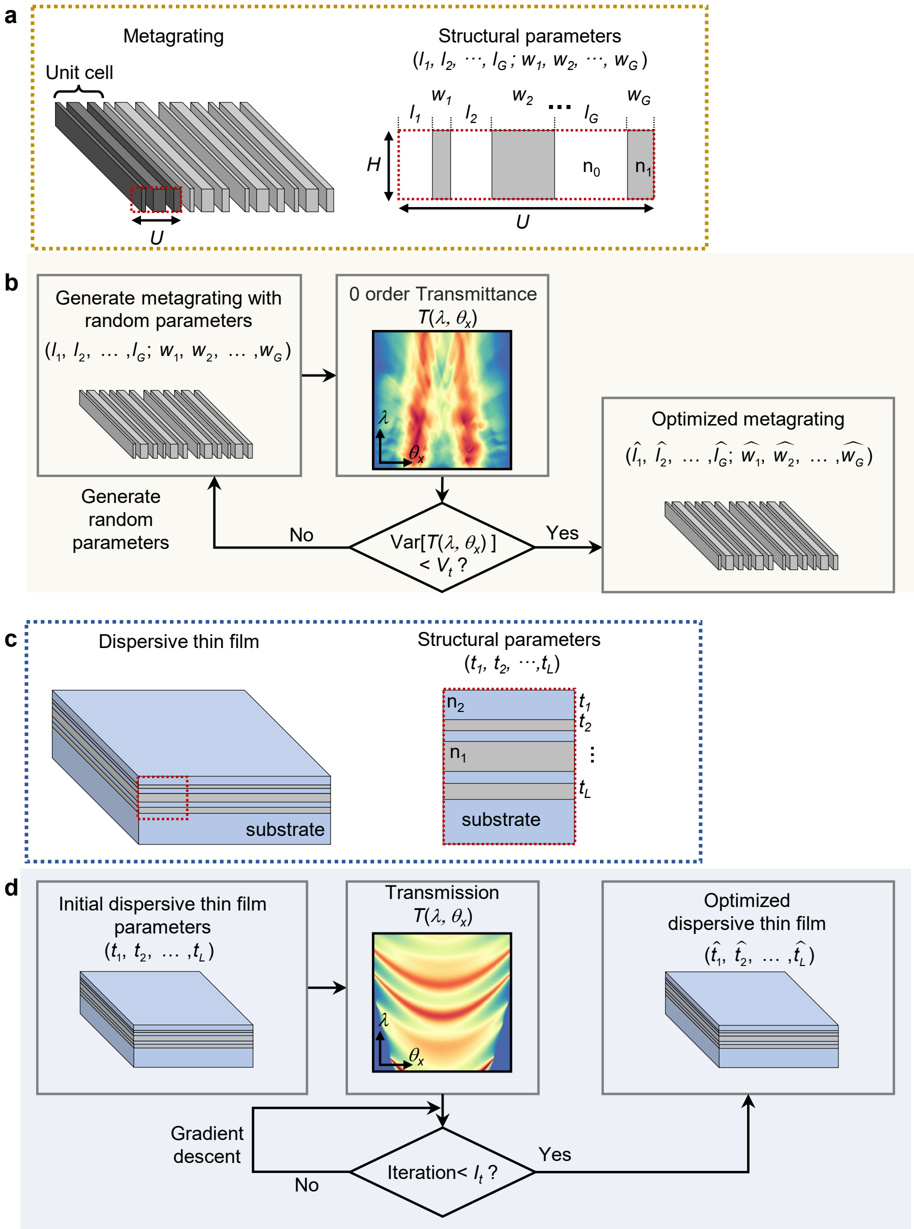

Fig. S3: **Design strategy to enhance the mode density. a** and **c**, Structural parameters of the metagrating layer and the thin film. **b**, Parameters for the metagrating are randomly generated until the corresponding system transmission map, $T(\lambda, \theta_x)$, meets the specified variance threshold. **d**, The multilayer thin film is iteratively refined using gradient descent to achieve the desired optical response.

high-density mode distribution across the (f, k_x) plane, responsive to various incident light conditions (λ, θ_x), resulting in a transmission profile that is globally uniform yet locally disordered. We evaluate this using the variance of the 0th-order transmission map, $\mathrm{var}[T_0(\lambda, \theta_x)]$, defined as:

$$\mathrm{var}\left[T_0(\lambda, \theta_x)\right] = \frac{1}{N_\lambda N_{\theta_x}} \sum_{i=1}^{N_\lambda} \sum_{j=1}^{N_{\theta_x}} \left[T_0(\lambda_i, \theta_{x,j}) - \bar{T}_0\right]^2, \tag{S1}$$

where $\overline{T_0}$ is the mean of T_0 over all (λ, θ_x). As shown in the flowchart (Fig. S3b), we iteratively generate random parameter sets $(l_1, l_2, \ldots, l_G; w_1, w_2, \ldots, w_G)$, compute the corresponding T_0, and repeat until the variance $\mathrm{var}(T_0)$ falls below a threshold V_t. The resulting optimized parameters are denoted $(\hat{l_1}, \hat{l_2}, \ldots, \hat{l_G}; \hat{w_1}, \hat{w_2}, \ldots, \hat{w_G})$.

For the thin film, layer thicknesses from the grating to the substrate are represented as $(t_1, t_2, \ldots, t_L)$ (Fig. S3c). Using a differentiable TMM simulator[32,33], we tailor these thicknesses to achieve a target response. The optimization targets a low variance in transmission by setting the desired response to 0.5 across the (λ, θ_x) range. Starting with an initial set of thicknesses $(t_1, t_2, \ldots, t_L)$, the TMM simulator computes $T_{\text{tf}}(\lambda, \theta_x)$, and the response is assessed via the mean square error loss:

$$\text{Loss}[T_{\text{tf}}(\lambda, \theta_x)] = \sum_{i=1}^{N_\lambda} \sum_{j=1}^{N_{\theta_x}} \left[T_{\text{tf}}\left(\lambda_i, \theta_{x,j}\right) - 0.5\right]^2 . \tag{S2}$$

Each thickness t_i is refined using gradient descent until a preset iteration limit is reached. The gradient is calculated via the chain rule:

$$\frac{\partial \text{Loss}}{\partial t_l} = \sum_{i=1}^{N_\lambda} \sum_{j=1}^{N_{\theta_x}} 2 \left[T_{\text{tf}}(\lambda_i, \theta_{x,j}) - 0.5\right] \frac{\partial T_{\text{tf}}(\lambda_i, \theta_{x,j}; t_1, \ldots, t_L)}{\partial t_l}. \tag{S3}$$

$$t_i^u = t_i^{u-1} - \eta \frac{\partial \, \text{Loss}[T_{\text{tf}}(\lambda, \theta_x)]}{\partial t_i^{u-1}}, \tag{S4}$$

where η is the learning rate.

2.3 Inducing coupling between multiple modes

Lastly, we induce coupling between the modes of the metagrating and those of the dispersive thin film. The zoom-in transmission maps presented in Fig. S4 demonstrate that stacking these two structures significantly increases the density of excitable modes. This indicates that their combination does not simply superimpose individual modes but rather introduces coupling between them. As demonstrated in Fig. S4, the E_y field distributions at selected excitation wavelengths and incident angles confirm this coupling: while the metagrating and dispersive thin film individually exhibit minimal E_y field response variations with changes in wavelength and angle, their stacked configuration displays distinctly different E_y field distributions.

Using these strategies, we construct the disordered-dispersion encoder (DDE), which introduces momentum-space disorder via a compact real-space structure. This results in a disordered transmission feature that varies with incident wavelength and angle (λ, θ_x). To illustrate this further, we calculate the transmission across various diffraction orders using the RCWA method. The grating equation is given by:

$$d_N \lambda = U \left[\sin(\theta_x) + \sin(\phi_x) \right], \tag{S5}$$

where $d_N = \pm 1, \pm 2, \pm 3, \ldots, \pm N_d$ is the diffraction order. θ_x and ϕ_x are the incident and exit angles, respectively. For a superlattice with $U = 3$ µm and a minimum wavelength of 400 nm, the structure supports up to $N_d = 4U/\lambda + 1 = 31$ diffraction orders.

Considering a practical range of $\theta_x \in [-60°, 60°]$ and the fiber's acceptance range of $\phi_x \in [-15°, 15°]$ when the DDE is equipped at the fiber end, only 17 diffraction orders contribute to the system response. These include the zeroth order and orders ± 1 through ± 8. Selected values of $E_{d_N}(\lambda, \theta_x)$ and $\phi_{d_N}(\lambda, \theta_x)$ are shown in Fig. S5a and Fig. S5b, respectively, with dark gray regions in Fig. S5b indicating the absence of corresponding diffraction orders for specific wavelengths and angles. The non-zero diffraction orders lack symmetry about the x-axis, resulting in an asymmetric transmission map when the DDE is equipped at the fiber end. This asymmetry is essential for enabling our single-fiber hyperspectral imager to effectively encode spatially asymmetric objects.

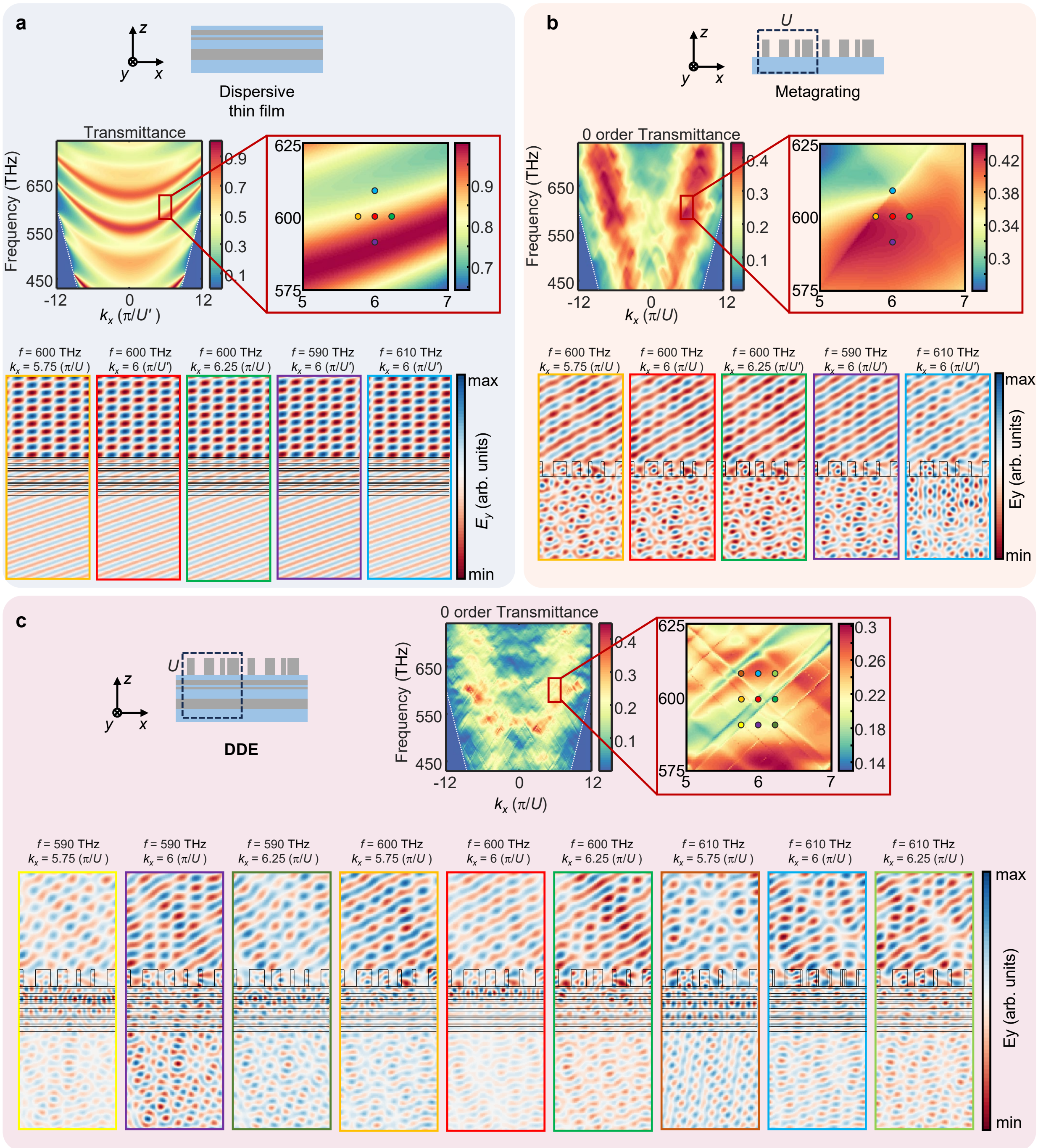

Fig. S4: **Zoom-in transmission diagram and E_y field distribution under adjacent incident parameters.** **a**, Slight perturbations in the incident light parameters excite a similar E_y field distribution in the dispersive thin film, resulting in insensitive and regular diffraction patterns. **b**, In the metagrating, the addition of selectable bands amplifies the differences in electric field distributions between adjacent modes. **c**, The proposed DDE structure leverages the coupling of dispersive thin film modes and metagrating modes, significantly increasing both the number and diversity of selectable modes. This leads to sensitive and disordered diffraction features even with minor variations in incident angle and wavelength.

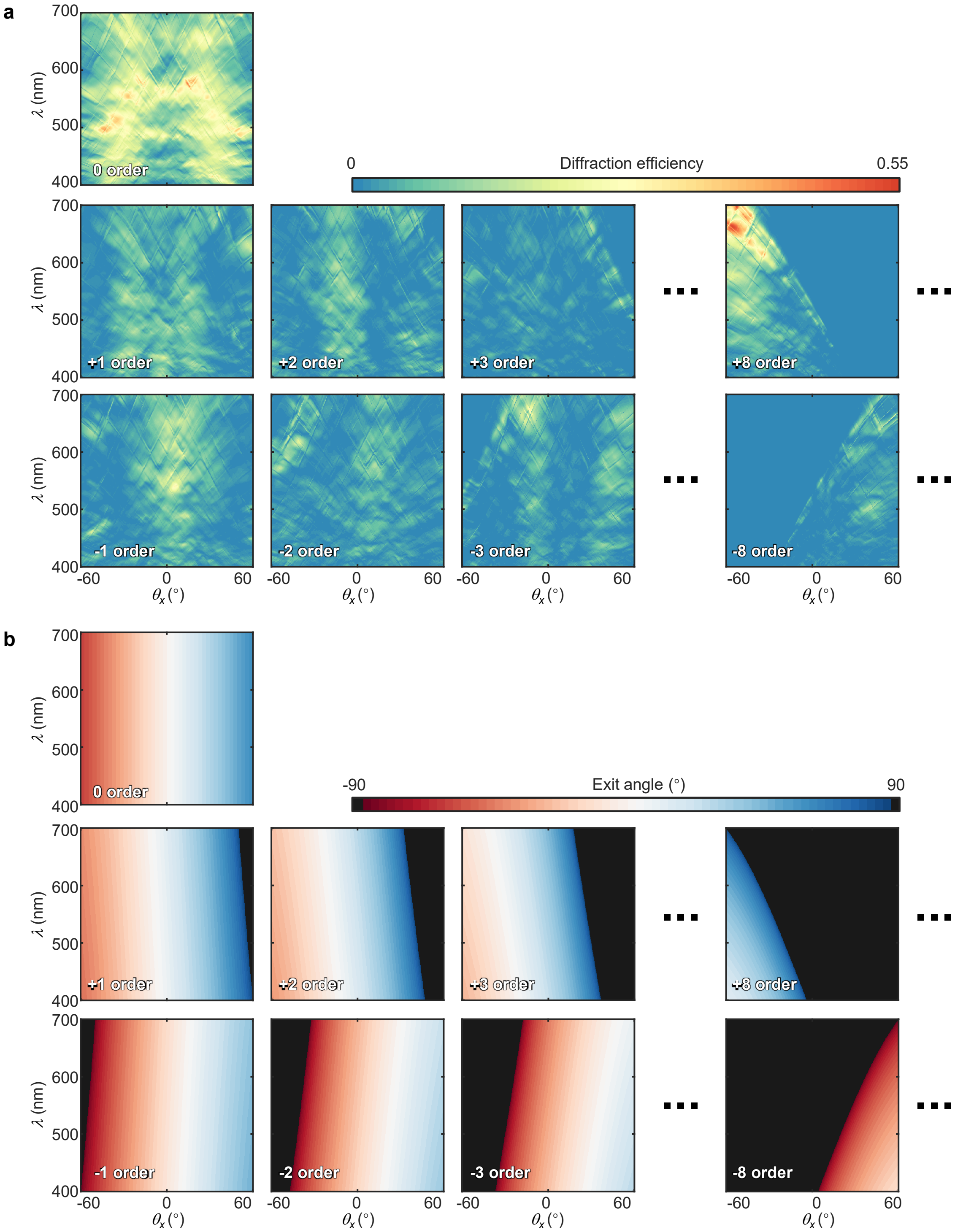

Fig. S5: **A selection of $E_i(\lambda, \theta_x)$ and $\phi_i(\lambda, \theta_x)$ values. a**, Diffraction efficiency $E_i(\lambda, \theta_x)$ of different orders. **b**, Exit angles $\phi_i(\lambda, \theta_x)$ in the air for different orders; the dark gray regions indicate that the diffracted beam cannot propagate to free space at the corresponding (λ, θ_x).

3 Eigenmodes and k-resolved DOS analysis

To directly demonstrate the high mode density and diversity of the DDE, we calculate its eigenmodes using the finite element method implemented in COMSOL Multiphysics. The band diagram presented in Fig. S6a reveals a dense distribution of bands. To distinguish real eigenmodes from spurious modes arising from numerical simulations, we define the local ratio for each mode as the squared electric field norm near the structure divided by the total squared field norm within the simulation domain:

$$\text{local ratio} = \frac{|E_{\text{near}}|^2}{|E_{\text{total}}|^2}, \tag{S6}$$

where real eigenmodes typically exhibit a high local ratio. In the band diagram, eigenmodes with higher local ratios are visualized using points with higher opacity, effectively highlighting the real modes.

Next, we statistically characterized the mode diversity of the DDE by calculating the k-resolved density of states (k-resolved DOS), defined as the number of modes per unit wavevector interval and per unit frequency interval:

$$k\text{-resolved DOS}(f_0, k_0) = \frac{\text{Mode number}_{\mathrm{d}f\mathrm{d}k}}{\mathrm{d}f\mathrm{d}k}, \tag{S7}$$

where Mode number$_{\mathrm{d}f\mathrm{d}k}$ represents the number of eigenmodes within the rectangle $(f_0, f_0 + \mathrm{d}f, k_0, k_0 + \mathrm{d}k)$. The results, shown in Fig. 2b in the main text, demonstrate high mode diversity across wavevectors in the first Brillouin zone and frequencies across the visible region, ensuring that the DDE exhibits disordered dispersion over a wide range of incident angles and wavelengths.

Figure S6b displays the electric fields of a selection of eigenmodes with closely spaced frequencies and wavevectors. Despite their similarity in frequency and wavevector, these eigenmodes show diverse electric field distributions due to the coupling between the leaky modes of the grating and the guided modes of the thin film. Consequently, slight perturbations in the wavelength or incident angle of the incoming light can excite a variety of modes in the DDE, contributing to the disordered response characteristic of its disordered dispersion.

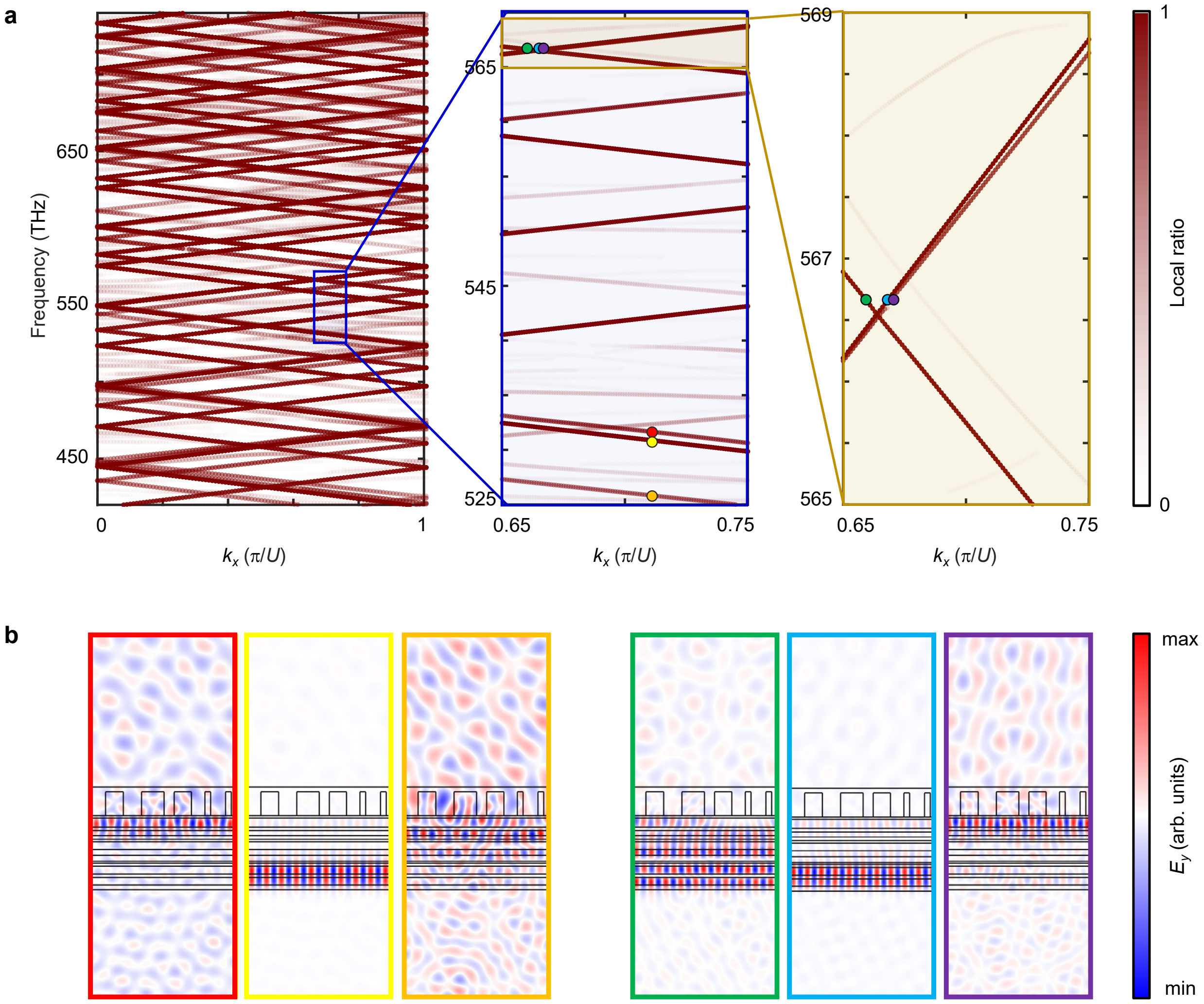

Fig. S6: **Band diagram and eigenmodes of the DDE. a**, The band diagram of the DDE. **b**, Selected modes with adjacent frequencies and wavevectors.

4 Calculation, characterization, and analyses of the system transmission map

4.1 Numerical calculation

We establish the relationship between $T(\lambda, \theta_x)$ and the dispersion properties of the DDE at the fiber input. As shown in Figs. S7a and S7b, $T(\lambda, \theta_x)$ is defined by the sum of diffraction efficiencies within the fiber's acceptance angle, each weighted by its coupling efficiency:

$$T(\lambda, \theta_x) = \sum_{i=1}^{N_d} E_i(\lambda, \theta_x)\, C\big(\phi_{x,i}\big), \tag{S8}$$

where N_d is the number of diffraction orders, and for each order i, E_i and $\phi_{x,i}$ denote its diffraction efficiency and exit angle (see Fig. S5). The coupling efficiency $C(\phi_x)$ is measured experimentally (flowchart in Fig. S7c).

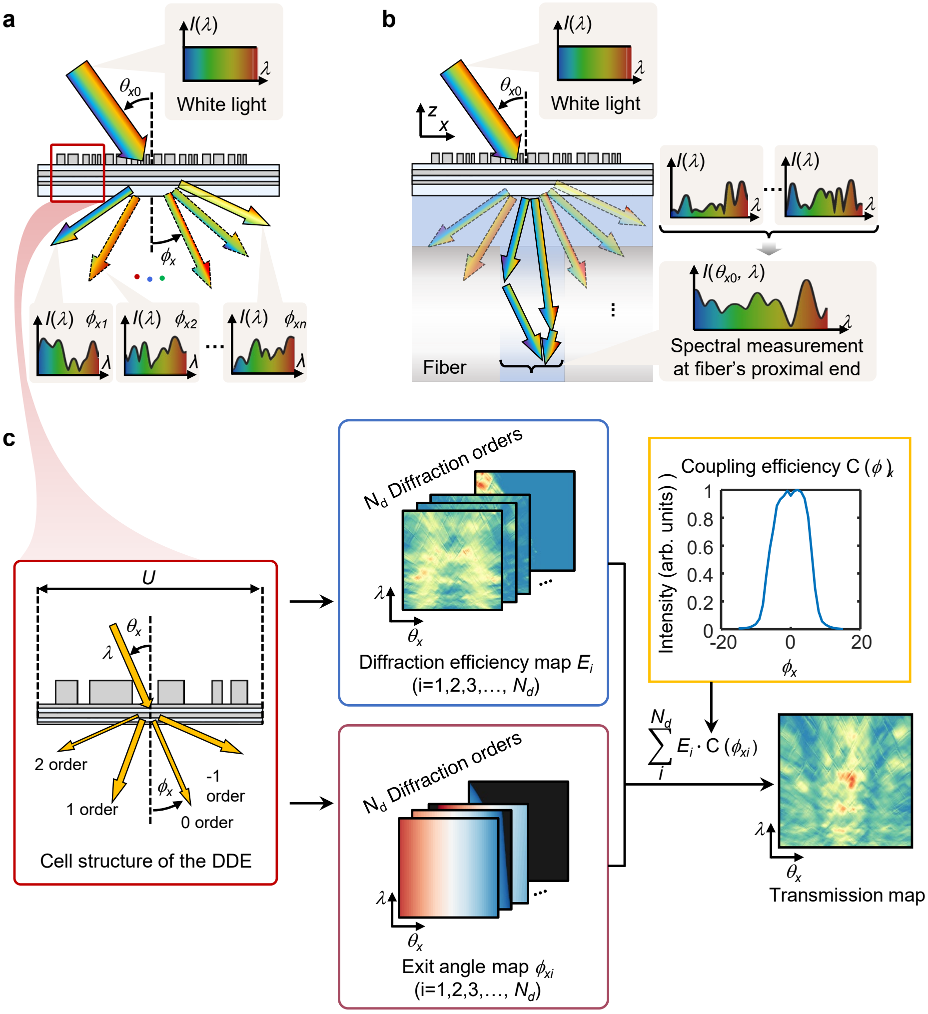

Fig. S7: **Numerical simulation of the transmission map. a**, The DDE diffracts incident light into various directions, with diffraction efficiencies exhibiting a complex distribution across different wavelengths and diffraction orders. **b**, In our design, the DDE is placed at the distal end of the fiber. Light exiting at angles ϕ within the fiber's acceptance range is collected and guided to the proximal end, where spatially averaged spectral detection is performed. **c**, By simulating the diffraction efficiency and exit angles for each diffraction order as a function of (λ, θ_x), the system transmission map is calculated.

4.2 Experimental characterization

To characterize the fabricated disordered-dispersion encoder and calibrate the system transmission map, we directed collimated broadband light with controllable incident angles (θ_x, θ_y) into the system, as shown in Fig. S8. Broadband light from a halogen lamp (OSL2IR, Thorlabs) was coupled into a 400 µm diameter multimode fiber (MMF) (XinRay). The light exiting the fiber was collimated using an achromatic lens (OLD1423-T2M, JCOPTIX). The fiber and achromatic lens were mounted on a rotation stage allowing precise control over the x and y directions.

The disordered-dispersion encoder with an aperture of 150 µm × 150 µm and a substrate thickness of 500 µm is placed adjacent to the end face of the fiber, which has a diameter of 400 µm (FCM1-SMA-400L, JCOPTIX). A polarizer is positioned between the light source and the metagrating to align the electric field with the grating's orientation. Light exiting the receiving fiber was detected using a spectrometer (HR6, Ocean Optics). By mechanically scanning the incident angles (θ_x, θ_y) of the light and normalizing the spectral data collected by the spectrometer against the spectral profile of the light source, the system transmission map $T(\lambda, \theta_x, \theta_y)$ is obtained.

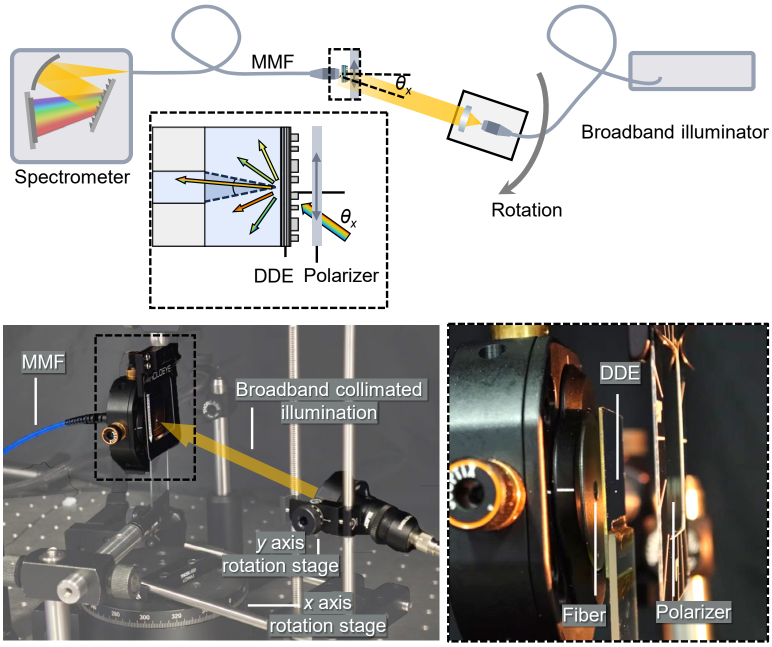

Fig. S8: **System transmission map measurement.** The system transmission map is calibrated by collecting the system response under collimated broadband light at different incident angles and normalizing it by dividing by the known light source spectrum.

4.3 Effect of setup configuration on the transmission map

In this section, we examine the factors influencing the system's transmission map $T(\lambda, \theta_x)$—including the fiber collection angle, key dimensional parameters of the metagrating and fiber, and polarization—to optimize its disordered characteristics.

The fiber coupling efficiency $C(\phi_x)$ depends on several factors (Fig. S9). In Fig. S9a, the numerical aperture (NA) sets the maximum acceptance angle, causing $C(\phi_x)$ to decrease as ϕ_x increases. Figure S9b shows the effect of the metagrating–fiber distance L_{sub} and fiber end-face diameter L_c: only light within the angular range $\left[-\arctan(L_c/2L_{sub}),\ \arctan(L_c/2L_{sub})\right]$ reaches the fiber. Conversely, Fig. S9c fixes the fiber diameter and varies the metagrating aperture L_a, so that coupling is limited to $\left[-\arctan(L_a/2L_{sub}),\ \arctan(L_a/2L_{sub})\right]$.

To illustrate how the shape of $C(\phi_x)$ affects $T(\lambda, \theta_x)$, Fig. S10 presents simulated transmission maps assuming Gaussian coupling efficiencies with different full widths at half maximum

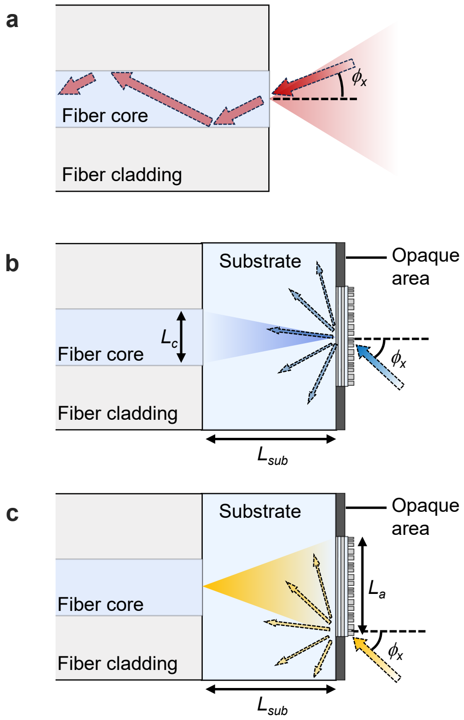

Fig. S9: **Parameters affecting coupling efficiency as a function of the fiber coupling angle. a**, Fiber's numerical aperture. **b** and **c**, Fiber end face aperture diameter L_c, metagrating aperture width L_a, and the distance between the metagrating and the fiber end face (the thickness of the metagrating substrate) L_{sub}.

(FWHM) C_{FWHM}. A narrow FWHM yields distinct, non-overlapping peaks from each diffraction order; as the FWHM increases, more orders are collected and their contributions to the transmission map broaden. The fifth column presents the experimentally measured coupling efficiency and the corresponding simulated transmission map.

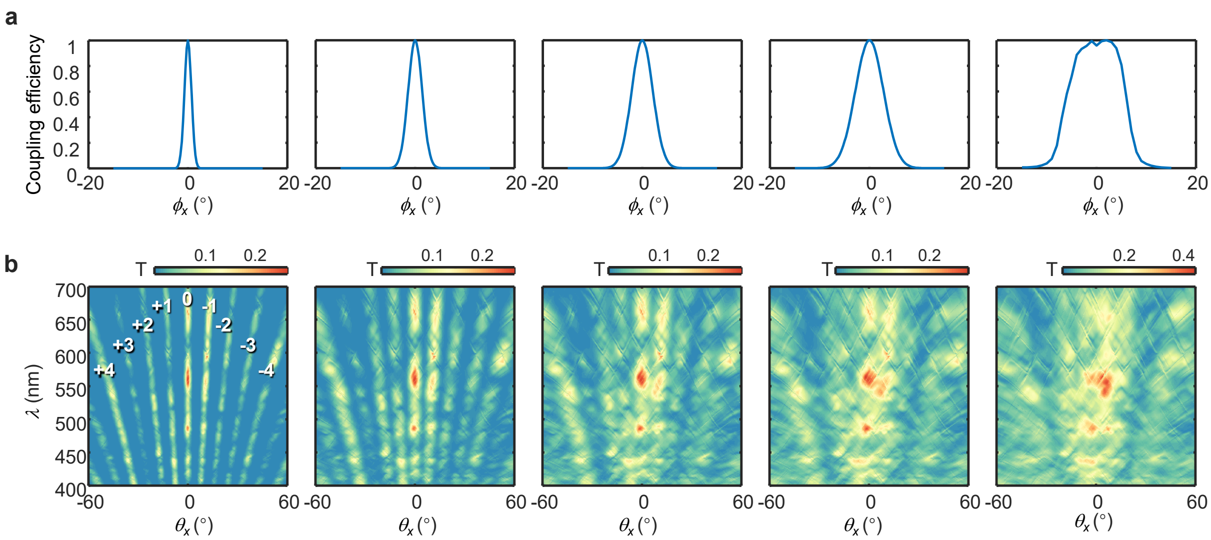

Fig. S10: **Diverse coupling efficiency and corresponding system transmission maps. a**, The first four columns represent simulations assuming that the coupling efficiency follows a Gaussian distribution, while the fifth column shows the experimentally measured values. **b**, The corresponding simulated transmission map.

Next, we compare transmission maps under orthogonal polarizations, $T_s(\lambda, \theta_x)$ and $T_p(\lambda, \theta_x)$, for s-polarized (electric field parallel to the grating) and p-polarized (electric field perpendicular) illumination, respectively (Fig. S11). The s-polarized map exhibits more pronounced disordered features. For unpolarized light, the overall map $T(\lambda, \theta_x)$ is a linear combination of T_s and T_p, showcasing that the system can image non-polarized objects.

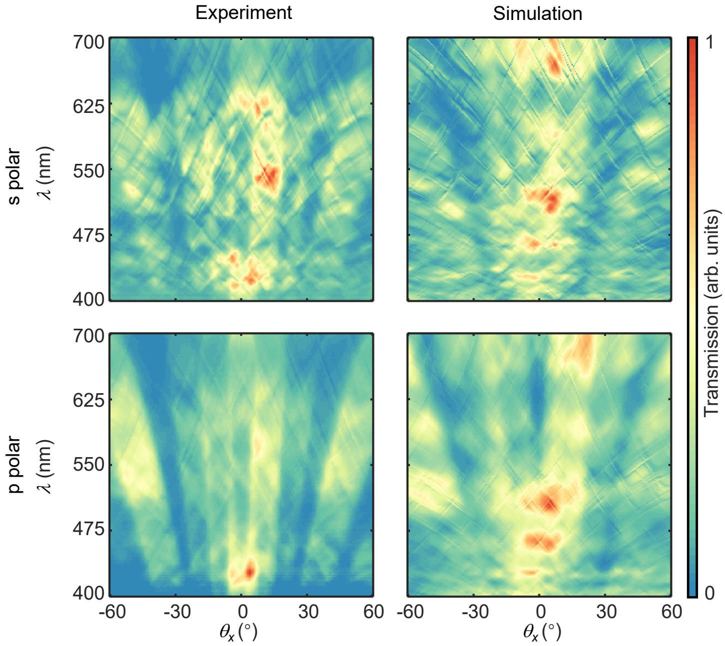

Fig. S11: **A comparison between the experimentally measured and simulated system transmission maps under different polarization states of incident light.** All the transmission maps are normalized.

Finally, we consider fabrication and assembly tolerances. Due to the disordered complex features of our system, small fabrication errors, such as slight variations in grating width, sidewall verticality, and thin-film uniformity, are amplified, leading to significant changes and local deviations in the response. Despite this, experimental results follow the simulated trends closely, with remaining discrepancies likely due to minor misalignments between the metagrating and fiber.

5 Analysis of encoding efficiency of the DDE and other optical encoding structures

In this section, we compare the encoding efficiency of three optical structures: the DDE, a periodic grating (PG), and a periodic thin film (TF). We first perform two quantitative analyses using the correlation coefficient and mutual coherence metrics, then compare the results of reconstruction simulations using each encoder.

Figure S12 shows schematics of the three structures and their transmission maps. The PG has a period of 0.5 μm, with 250 nm grooves and ridges, and a height of 250 nm, fabricated in silicon nitride on a quartz substrate. The TF consists of five alternating Si_3N_4/SiO_2 layers on quartz, each 100 nm thick. As the second column of Fig. S12 illustrates, the simple PG fails to produce a disordered transmission map, while the TF cannot provide transverse momentum to the incident light and thus does not provide angle-dependent modulation.

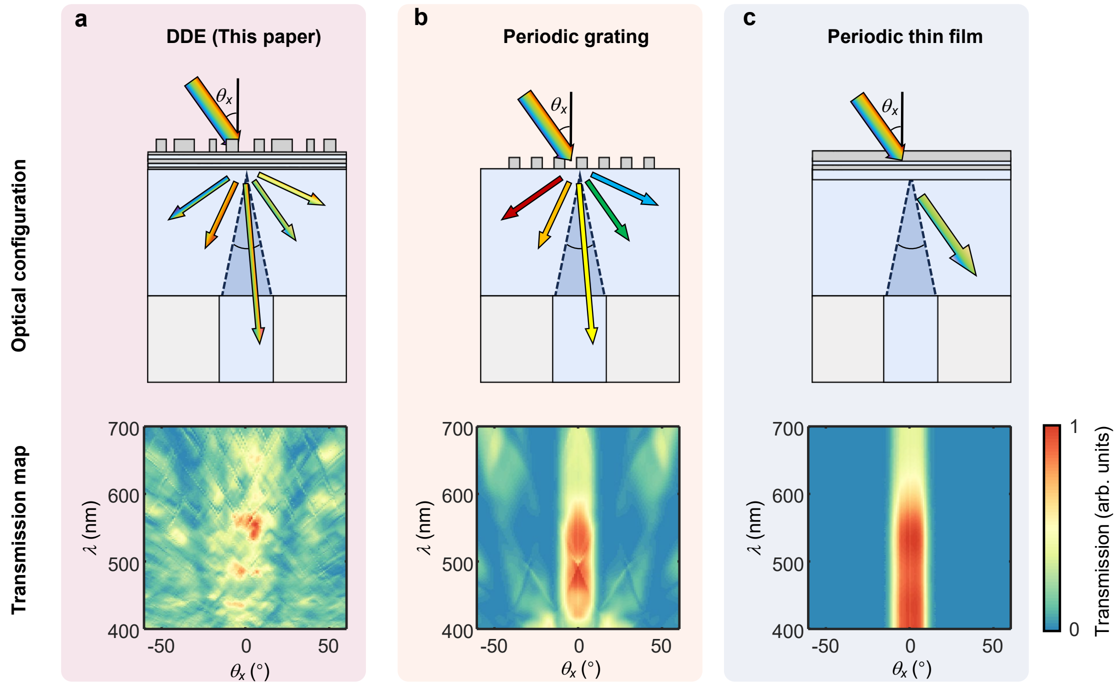

Fig. S12: **Schematics of different encoder structures and their transmission maps. a**, The disordered-dispersion encoder (DDE) proposed in this paper. **b**, The periodic grating (PG). **c**, The periodic thin film (TF).

5.1 Correlation coefficient (CC) analysis

We first examine the inter-θ and inter-λ correlation coefficients (CC). Lower inter-θ CC and inter-λ CC indicate superior encoding capability in the angular and spectral dimensions, respectively. The CC is computed via the Pearson correlation coefficient:

$$\mathrm{CC}(\theta_1, \theta_2) = \frac{1}{N_\lambda - 1} \sum_{i=1}^{N_\lambda} \left(\frac{T_i^{\theta_1} - \overline{T^{\theta_1}}}{\sigma_{T^{\theta_1}}} \right) \left(\frac{T_i^{\theta_2} - \overline{T^{\theta_2}}}{\sigma_{T^{\theta_2}}} \right), \tag{S9}$$

$$\mathrm{CC}(\lambda_1, \lambda_2) = \frac{1}{N_\theta - 1} \sum_{i=1}^{N_\theta} \left(\frac{T_i^{\lambda_1} - \overline{T^{\lambda_1}}}{\sigma_{T^{\lambda_1}}} \right) \left(\frac{T_i^{\lambda_2} - \overline{T^{\lambda_2}}}{\sigma_{T^{\lambda_2}}} \right), \tag{S10}$$

where N_λ and N_θ are the numbers of discrete channels in the wavelength and incident-angle dimensions. T^{θ_1} and T^{λ_1} denote slices of the transmission map at $\theta = \theta_1$ and $\lambda = \lambda_1$, respectively; $\overline{T^\theta}$ and σ_{T^θ} represent the mean and standard deviation of a slice.

Figure S13 shows the inter-θ CC and inter-λ CC for the three encoders. All CC matrices have unity on the diagonal, since each vector is perfectly correlated with itself. Low correlation of the transmission map appears as small off-diagonal values. The PG offers limited diversity in both dimensions, while the TF provides limited angular diversity and relatively simple spectral diversity. In contrast, the DDE exhibits the lowest inter-θ CC and inter-λ CC across all parameters.

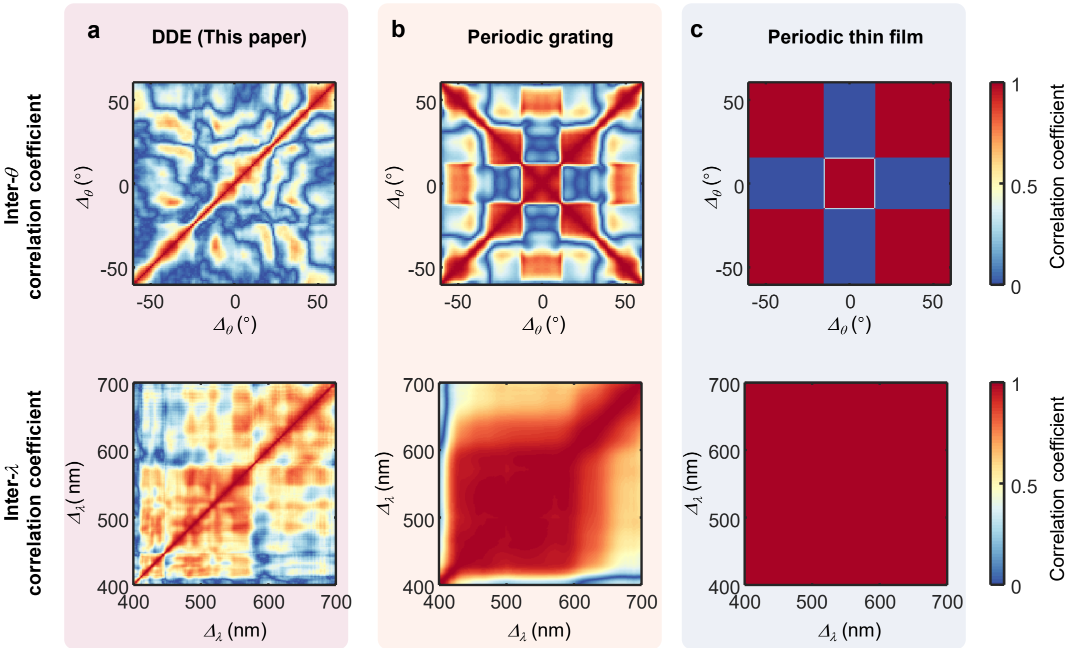

Fig. S13: **Inter-θ CC and inter-λ CC of the three transmission maps. a**, The disordered-dispersion encoder proposed in this paper. **b**, The periodic grating. **c**, The periodic thin film.

5.2 Mutual coherence analysis

We then assess compressive encoding efficiency via mutual coherence. According to compressive sensing theory, a lower $\mu(\boldsymbol{S}, \boldsymbol{\Psi})$ means fewer measurements are required to reconstruct the object with high probability, where $\boldsymbol{S}$ is the sampling matrix and $\boldsymbol{\Psi}$ is the sparse basis. Given a fixed $\boldsymbol{\Psi}$, a lower μ indicates better encoding efficiency. Mutual coherence is defined as

$$\mu(\boldsymbol{S}, \boldsymbol{\Psi}) = \sqrt{N_\lambda N_\theta} \max_{i,j} \left| {s_i}^T \psi_j \right|, \tag{S11}$$

where s_i^T and ψ_j are the i-th row of $\boldsymbol{S}$ and the j-th column of $\boldsymbol{\Psi}$, respectively.

Figure S14 illustrates the computation flow of μ. We form $\boldsymbol{S}$ by discretizing $T(\lambda, \theta_x)$ into an $N_\lambda \times N_\theta$ matrix and assigning each row to a different λ. To construct $\boldsymbol{\Psi}$, we randomly extract n (λ, x) and (λ, y) slices from hyperspectral images in the CAVE database[34], vectorize and concatenate them into an $N_\lambda N_\theta \times n$ matrix, then apply principal component analysis to obtain a sparse $N_\lambda N_\theta \times N_\lambda N_\theta$ basis. We average the top 20 values of $|s_i^T \psi_j|$ to mitigate discrete-channel effects.

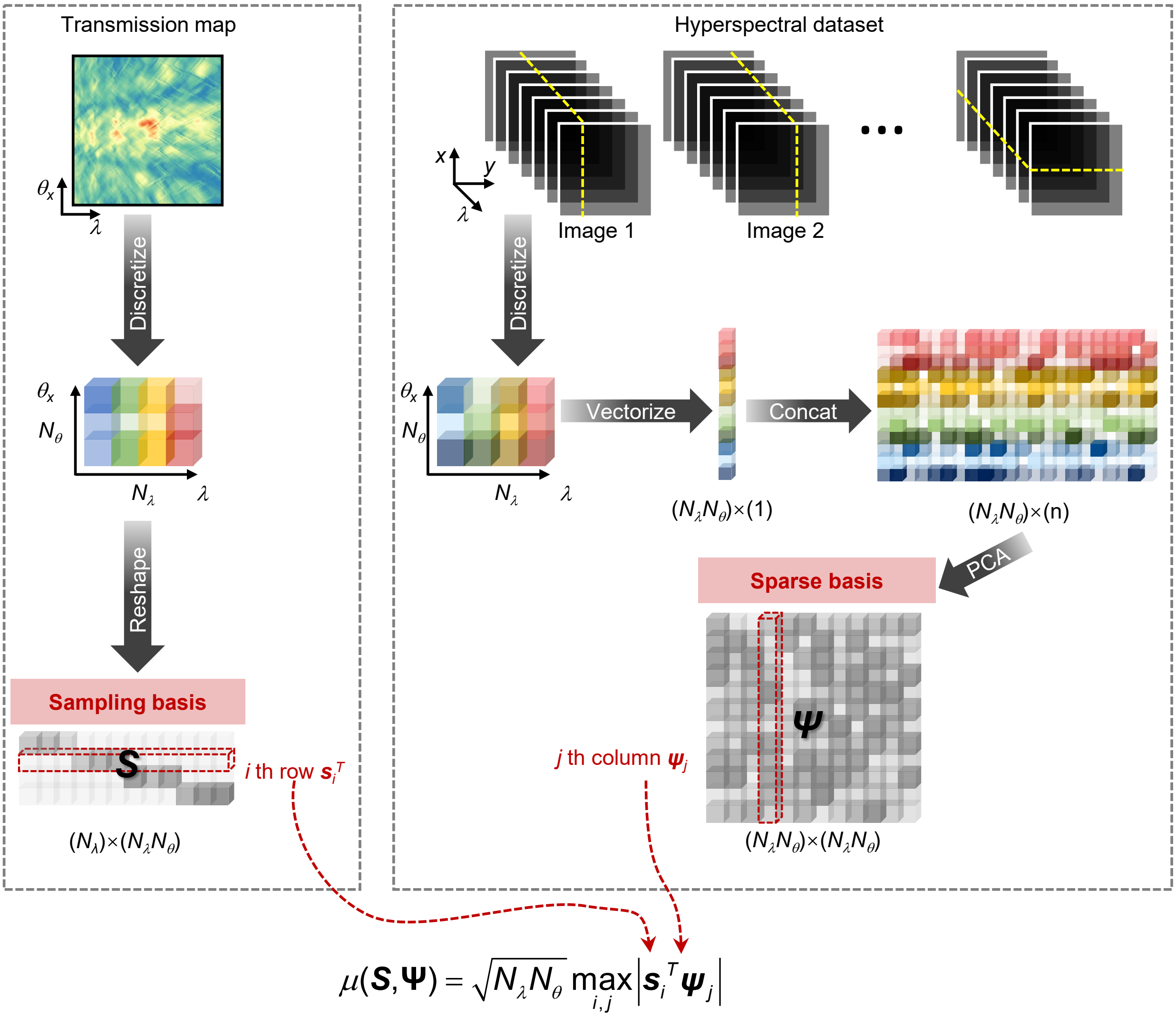

Fig. S14: **Workflow of calculating mutual coherence** $\mu(S, \Psi)$. PCA, principal component analysis.

As shown in Fig. S15, for all three structures, mutual coherence increases with N_θ (the compression ratio), indicating a more underdetermined problem that demands more spectral measurements. The DDE consistently achieves the lowest μ across all N_θ and N_λ, demonstrating its superior encoding efficiency.

5.3 Image reconstruction analysis

Finally, we perform reconstruction simulations to validate encoding performance (Fig. S16). We use colored handwritten digits from the MNIST dataset[35] as hyperspectral objects and introduce y-dimensional diversity by sweeping along the y-axis rather than rotating about the z-axis in the main text. Simple encoders (PG and TF) fail to capture structural information accurately. In contrast, transmission maps with stronger disordered features enable

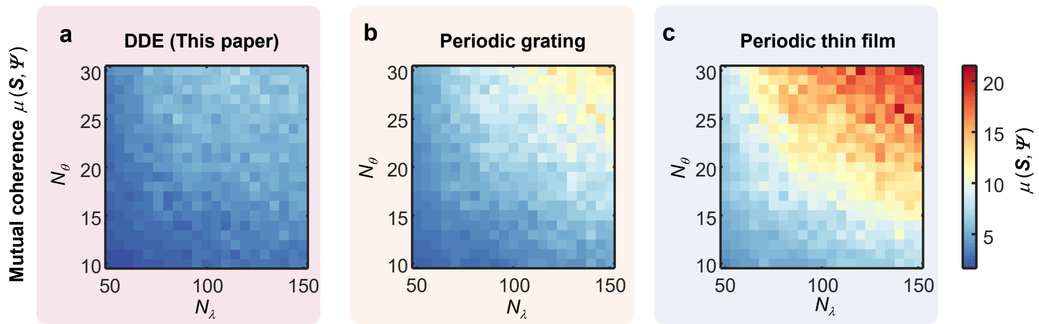

Fig. S15: **Mutual coherence of the three transmission maps. a**, The disordered-dispersion encoder proposed in this paper. **b**, The periodic grating. **c**, The periodic thin film.

high-resolution, high-fidelity reconstructions. We evaluate similarity between the reconstructed and ground-truth images using peak signal-to-noise ratio (PSNR) and structural similarity index (SSIM), respectively defined as:

$$\mathrm{PSNR}(a, b) = 10 \log_{10}\Big(\frac{\mathrm{MAX}^2}{\mathrm{MSE}}\Big), \tag{S12}$$

$$\mathrm{SSIM}(a, b) = \frac{(2\mu_a\mu_b + C_1)(2\sigma_{ab} + C_2)}{(\mu_a^2 + \mu_b^2 + C_1)(\sigma_a^2 + \sigma_b^2 + C_2)}, \tag{S13}$$

where MAX is the maximum possible pixel value of the image, $\mathrm{MSE} = \frac{1}{N}\sum_{i=1}^{N}\big(a_i - b_i\big)^2$ is the mean squared error between the reconstructed image a and the ground truth image b over N pixels, μ_a and μ_b are the mean intensity values of images a and b, respectively, σ_a^2 and σ_b^2 are the variances of images a and b, σ_{ab} is the covariance between images a and b. C_1 and C_2 are small stabilization constants.

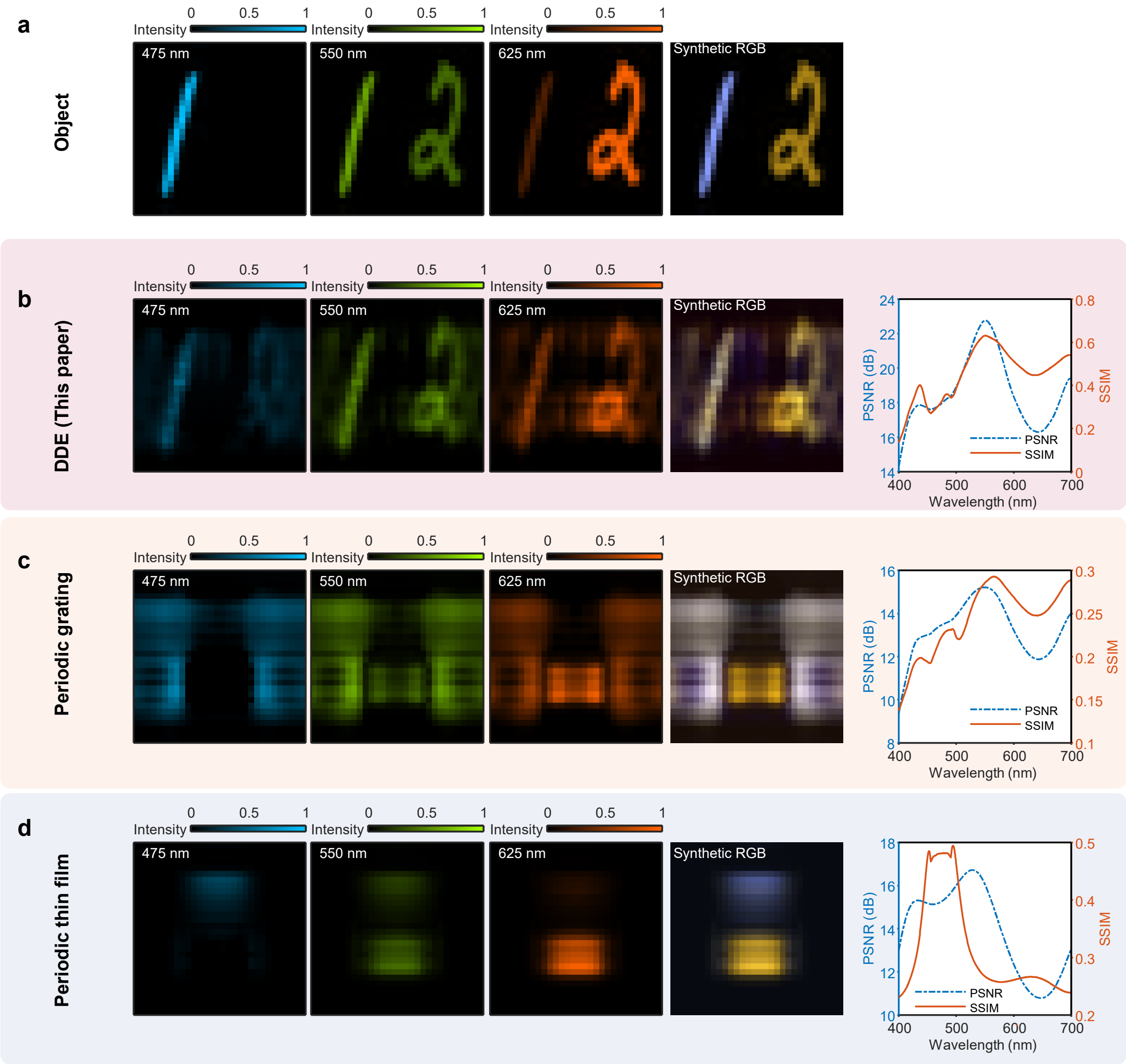

Fig. S16: **Reconstruction results with different encoder configurations. a**, The ground-truth hyperspectral object. **b**, The disordered-dispersion encoder proposed in this paper. **c**, The periodic grating. **d**, The periodic thin film.

5.4 Comparison with diffuser-type encoders

The DDE is fundamentally different from conventional diffuser-type encoders. Here, a diffuser-type encoder refers to a real-space disordered phase or amplitude screen, such as a ground-glass diffuser or a disordered metasurface. Such a diffuser modulates the incident field through spatially varying transmission. For an incident plane wave, it generates a far-field angular speckle distribution. Under a small change in the incident angle, the speckle pattern mainly shifts in output angle rather than changing into an independent pattern, corresponding to the memory effect, as schematically shown in Fig. S17a.

In our fiber-tip encoding configuration, this mechanism leads to a trade-off between photon throughput and angular encoding diversity. The transmission map of a system with a diffuser-type encoder is the angular speckle intensity integrated over the fiber acceptance angle,

$$T_{\text{diff}}(\lambda, \theta_{\text{in}}) = \int_{\Omega_{\text{fiber}}} I_{\text{diff}}(\lambda, \phi_{\text{out}}; \theta_{\text{in}}) C(\phi_{\text{out}})\, d\phi_{\text{out}}, \tag{S14}$$

where $I_{\text{diff}}(\lambda, \phi_{\text{out}}; \theta_{\text{in}})$ is the far-field speckle intensity distribution generated by the diffuser for wavelength λ and incident angle θ_{in}, and $C(\phi_{\text{out}})$ is the angle-dependent coupling efficiency of the fiber. Because of the memory effect, changing θ_{in} mainly translates I_{diff} along ϕ_{out}. If $C(\phi_{\text{out}})$ is narrow, the fiber samples only one or a few speckle grains, so T_{diff} can fluctuate with θ_{in}, but the collected photon flux is low. If $C(\phi_{\text{out}})$ is broad, many speckle grains are averaged during the integration, and translating the speckle pattern produces only a weak change in the collected signal. The resulting transmission map therefore becomes smooth and highly correlated.

In contrast, our DDE is designed to generate disorder directly in the wavevector domain, as schematically shown in Fig. S17b. The wavelength- and angle-dependent response arises from diffraction and modal coupling, so changing the incident angle does not merely translate a fixed speckle pattern. Instead, nearby incident angles can excite different spectral-angular responses, suppressing the angular-memory-effect-induced correlation. Therefore, the DDE can maintain low-correlation spectral-angular encoding under a larger useful collection angle, providing a favorable balance between encoding diversity and optical throughput for single-fiber spectral-only measurements.

We further simulate a representative diffuser to illustrate this trade-off, as shown in Fig. S17c. The diffuser has a 150 µm × 150 µm aperture and a 1 µm pixel pitch, and is modeled as fused-silica structures with heights uniformly distributed from 0 to 4 µm. With a small fiber coupling-angle FWHM of 0.5°, the diffuser-based transmission map retains random fluctuations, but the absolute photon efficiency is only 0.016%. When the fiber coupling-angle FWHM is increased to 10°, the absolute efficiency increases to 5.2%, but the angular speckle is averaged and the transmission map becomes smooth. By comparison, under the same 10° coupling-angle FWHM, the DDE maintains a complex spectral-angular transmission map while achieving a comparable absolute efficiency of 4.8%.

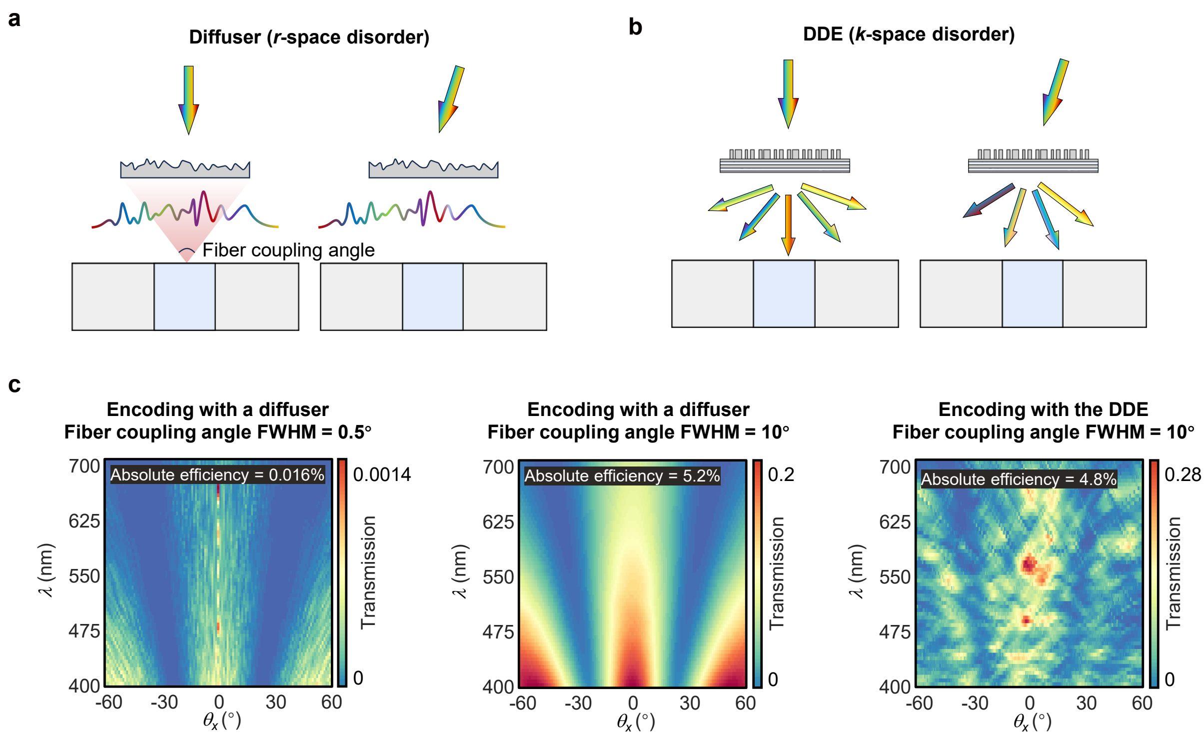

Fig. S17: Comparison between diffuser-type and DDE-type encoders. **a**, A diffuser is a real-space-disordered encoder. A change in incident angle mainly shifts the far-field speckle pattern, leading to correlated angular responses within the memory-effect range. **b**, The DDE generates disorder in the wavevector domain. Different incident angles excite different diffraction/modal responses, producing low-correlation spectral-angular encoding. **c**, Simulated transmission maps under different fiber coupling-angle FWHMs. For the diffuser-type encoder, a small coupling-angle FWHM of 0.5° preserves random fluctuations but gives a low absolute efficiency, whereas a larger coupling-angle FWHM of 10° increases the efficiency but smooths the transmission map. Under the same 10° coupling-angle FWHM, the DDE maintains a complex spectral-angular transmission map with a comparable absolute efficiency.

6 Analysis of single-shot 2D hyperspectral imaging

The current DDE design generates disordered dispersion in the (f, k_x) space, corresponding to disordered modulation in the (λ, θ_x) domain, while the encoding capability along θ_y remains limited, as shown by the measured transmission-map slices in Fig. S18a. Therefore, the present device supports single-shot reconstruction mainly in the (λ, θ_x) domain, and the second spatial dimension in the current 2D experiments is introduced by rotation or scanning.

A direct route toward single-shot 2D hyperspectral imaging is to extend the DDE to two-dimensional wavevector-space disorder. For example, the 1D metagrating can be replaced by a 2D aperiodic or supercell metasurface on the dispersive multilayer film. Such a structure can provide diffraction channels along both k_x and k_y, whose coupling with the dispersive multilayer modes can generate a disordered transmission map. A more systematic strategy is to inverse-design the encoder by directly optimizing $T(\lambda, \theta_x, \theta_y)$ using task-oriented figures of merit (FoM), such as mutual coherence, information capacity, optical throughput, noise robustness, fabrication tolerance, or end-to-end reconstruction loss. Such FoM-guided inverse design may further improve both encoding diversity and photon efficiency.

To validate the feasibility of this route, we use an ideal random encoder as an upper-bound model to examine whether sufficiently decorrelated responses in the $(\lambda, \theta_x, \theta_y)$ domain can support single-shot 2D hyperspectral reconstruction. We simulated the transmission map using randomly distributed elements ranging from 0 to 1, for various numbers of wavelength channels, while discretizing θ_x and θ_y into 20 channels each, as shown in Fig. S18b. The reconstruction results, shown in Fig. S18 c-f, indicate that as the number of available wavelength channels increases, the measured raw spectral data contain richer scene information, thereby improving the possibility of accurate reconstruction. Furthermore, enhancing the disordered nature of the transmission map can significantly boost reconstruction quality, providing valuable design insights for future encoding devices.

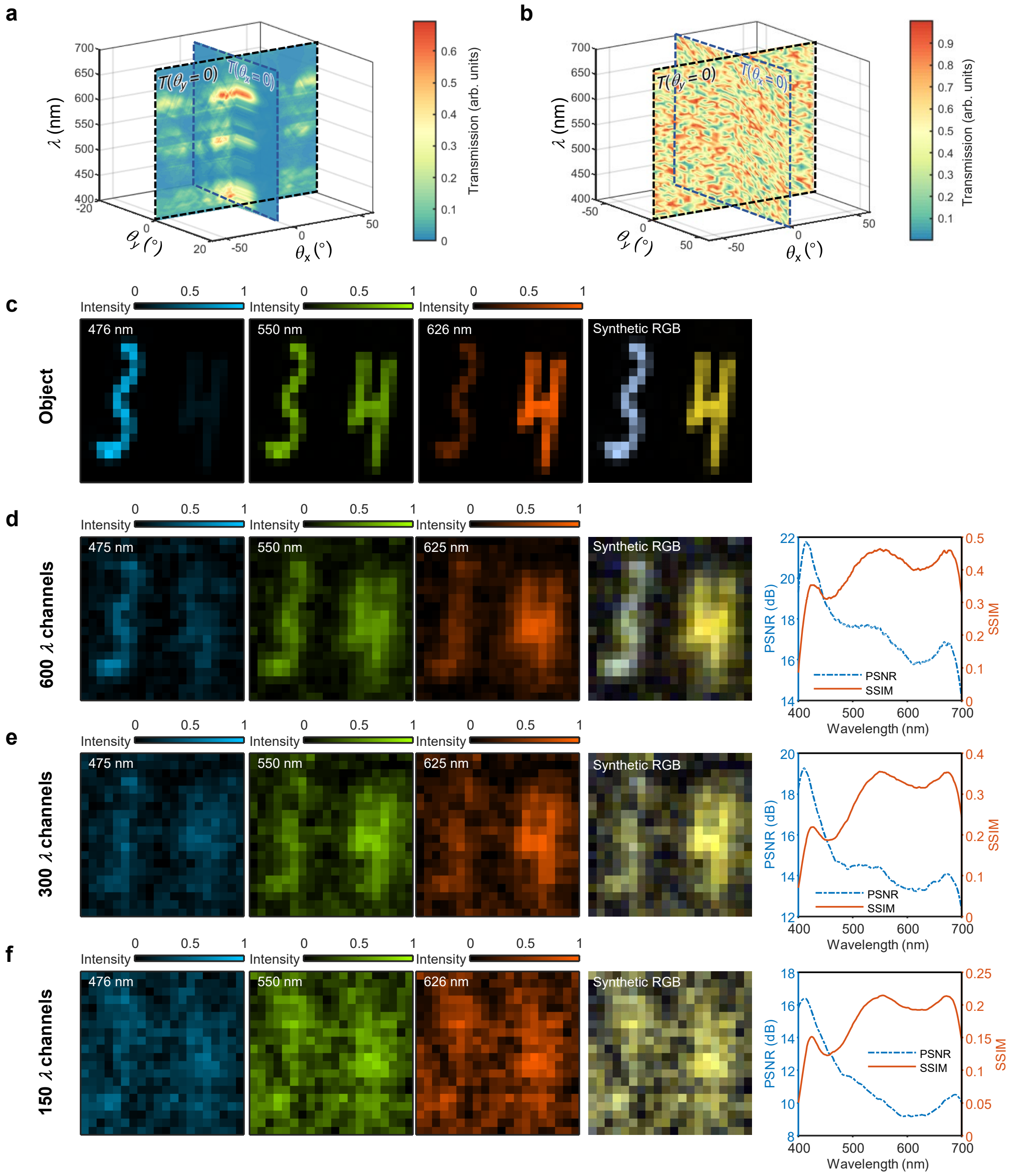

Fig. S18: **Analysis of single-shot 2D hyperspectral imaging. a**, The transmission map slices of the DDE at $\theta_x = 0$ and $\theta_y = 0$. **b**, The transmission map slices of an ideal random encoder at $\theta_x = 0$ and $\theta_y = 0$. **c-f**, Ground truth object and the reconstruction results with different available λ channels.

7 1D hyperspectral imaging experiments

7.1 Experiment setup

In this section, we provide a detailed description of the imaging tests performed with 1D objects $O(\lambda, \theta_x)$. The imaging module, consisting of a polarizer, DDE, MMF, and spectrometer, is configured identically to the calibration setup described in Fig. S8. The 1D hyperspectral imaging experimental setups are shown in Fig. S19.

To construct 1D hyperspectral samples with customized (λ, θ_x) distributions, broadband illumination (OSL2COL, Thorlabs) is collimated and sequentially passed through a diffuser (DG10-120-MD, Thorlabs), a slit aperture, and a color filter. The sample is mounted on a rotation stage that allows precise control of its orientation in the x direction. The diffuser ensures approximately uniform illumination intensity across incident angles. The incident angle distribution is controlled using the slit aperture and the rotational stage, while the λ distribution is adjusted by changing the filters. In the main text (Fig. 3a, 3b, 3d), the three sample, O1, O2, and O3, correspond to a single slit with a 550 nm longpass filter (Edmund), a single slit with a blue filter, and a double slit with no filter, respectively. The single slit provided uniform object light over a 5.5° span. The double slit configuration generated object light with each slit having an angular span of 2.7° and an angular separation of 2.7° between the slits.

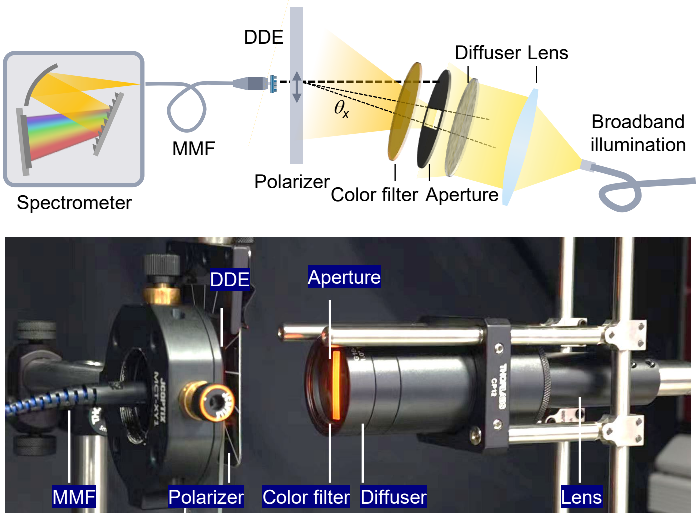

Fig. S19: **Experimental setup for spectral-angular imaging.** The incident light with a spectral-angular distribution is generated by passing broadband illumination through a diffuser, an aperture, and a color filter. An incident angle range of $-60°$ to $60°$ and different spectral distributions are demonstrated.

7.2 Reconstruction algorithm

The reconstruction of 1D hyperspectral images is schematically illustrated in Fig. 3c. The unknown object $\boldsymbol{o}$ is reconstructed by solving the basis-pursuit problem Eq. S15, according to the compressive sensing theory,

$$\begin{aligned} \hat{\boldsymbol{o}} &= \underset{\boldsymbol{o}}{\operatorname{argmin}} \left\| \boldsymbol{\Psi}^{-1} \boldsymbol{o} \right\|_1 \\ \text{s.t.} \quad \boldsymbol{S}\boldsymbol{o} &= \boldsymbol{m}, \end{aligned} \tag{S15}$$

where $\|\cdot\|_1$ is the l_1 norm. Note that $\boldsymbol{\Psi}$ here is different from the PCA-derived sparse basis used for the mutual-coherence analysis in Section 5.2. For reconstruction, we instead adopt simplified gradient-based sparsifying transforms along the spatial and spectral dimensions. The basis pursuit problem can be equivalently solved by minimizing the target function

$$\hat{\boldsymbol{o}} = \underset{\boldsymbol{o}}{\operatorname{argmin}} \underbrace{\frac{1}{2}\|\boldsymbol{S}\boldsymbol{o} - \boldsymbol{m}\|_2^2}_{\text{Fidelity term } F(\boldsymbol{o})} + \underbrace{\left\|\boldsymbol{\Psi}^{-1}\boldsymbol{o}\right\|_1}_{\text{Prior term } R(\boldsymbol{o})} . \tag{S16}$$

Specifically, considering the differing statistical distributions of the hyperspectral cube along the spatial and spectral axes, the prior term is given by $\left\|\boldsymbol{\Psi}^{-1}\boldsymbol{o}\right\| = \alpha \left\|\boldsymbol{\Psi_{xy}}^{-1}\boldsymbol{o}\right\|_1 + \beta \left\|\boldsymbol{\Psi_\lambda}^{-1}\boldsymbol{o}\right\|_2$. Here, l_1 and l_2 norms are applied to the spatial dimensions θ_x, θ_y and spectral dimension λ, respectively, with α and β as hyperparameters. Following the fast iterative shrinkage-thresholding algorithm (FISTA)[36,37], the convex minimization problem Eq. S16 can be solved by iteratively updating $\boldsymbol{o}$ according to the fidelity term $F(\boldsymbol{o})$ and the prior term (or regularization term) $R(\boldsymbol{o})$.

The pseudocode of the algorithm is shown in Algorithm 1. Since $F(\boldsymbol{o})$ is differentiable, the fidelity term $F(\boldsymbol{o})$ is updated with gradient descent, the k-th update is formulated as

$$\boldsymbol{o}_{k+1} = \boldsymbol{o}_k - \gamma \nabla_{\boldsymbol{o}} F(\boldsymbol{o}_k), \tag{S17}$$

$$\nabla_{\boldsymbol{o}} F(\boldsymbol{o}_k) = \boldsymbol{S}^T(\boldsymbol{S}\boldsymbol{o}_k - \boldsymbol{m}), \tag{S18}$$

where γ is the step size, $(\cdot)^T$ represents the transpose.

Algorithm 1 FISTA for hyperspectral image decoding

Initialization: $\boldsymbol{o}_0 \Leftarrow \mathbf{0},\ t_1 \Leftarrow 1$
for $k = 1, \cdots, K$ **do**
  Fidelity update: $\boldsymbol{u}_k \Leftarrow \boldsymbol{o}_{k-1} - \gamma \nabla_{\boldsymbol{o}} F(\boldsymbol{o}_{k-1})$
  Prior update: $\boldsymbol{v}_k \Leftarrow \operatorname{prox}_\gamma(\boldsymbol{u}_k)$
  Update t: $t_{k+1} \Leftarrow \frac{1+\sqrt{1+4t_k^2}}{2}$
  Update $\boldsymbol{o}_k$*:* $\boldsymbol{o}_k \Leftarrow \boldsymbol{v}_k + \frac{t_k - 1}{t_{k+1}}(\boldsymbol{v}_k - \boldsymbol{v}_{k-1})$
end for
Output: $\hat{\boldsymbol{o}} \Leftarrow \boldsymbol{o}_K$ (Reconstructed image)

The prior term $R(\boldsymbol{o})$ is not differentiable everywhere, therefore the prior update is implemented with a proximal solver Algorithm 2 instead. The proximal solver coincides with a denoising problem Eq. S19, which is solved with the fast gradient projection method[36,37].

$$\mathrm{prox}_{\gamma}(\boldsymbol{o}) = \underset{\boldsymbol{v}}{\mathrm{argmin}}\, \|\boldsymbol{o} - \boldsymbol{v}\|_2 + \gamma R(\boldsymbol{v}). \tag{S19}$$

In Algorithm 2, $\mathcal{P}_C$ denotes a projection operator that constrains the reconstruction to $[0, \infty)$. Specifically, this operator is represented by the pixel-wise function $\mathcal{P}_C(\boldsymbol{x}) = \max(\boldsymbol{x}, 0)$.

Algorithm 2 Proximal solver $\hat{\boldsymbol{v}} = \mathrm{prox}_{\gamma}(\boldsymbol{u})$

Require: Input $\boldsymbol{u}$, γ
Ensure: Output $\hat{\boldsymbol{v}}$
1: **Initialization:** $\boldsymbol{v}_1 \Leftarrow \boldsymbol{0}, \boldsymbol{w}_0 \Leftarrow \boldsymbol{0},\ t_1 \Leftarrow 1$
2: **for** $k = 1, \cdots, K_p$ **do**
3: *Compute* $\boldsymbol{w}_k$: $\boldsymbol{w}_k \Leftarrow \boldsymbol{v}_k + \frac{1}{8\gamma}\boldsymbol{\Psi^{-1}}\left[\mathcal{P}_C(\boldsymbol{u} - \gamma(\boldsymbol{\Psi^{-1}})^{\boldsymbol{T}}\boldsymbol{v}_k)\right]$
4: *Update* t: $t_{k+1} \Leftarrow \frac{1+\sqrt{1+4t_k^2}}{2}$
5: *Update* $\boldsymbol{v}_{k+1}$: $\boldsymbol{v}_{k+1} \Leftarrow \boldsymbol{w}_k + \frac{t_k - 1}{t_{k+1}}(\boldsymbol{w}_k - \boldsymbol{w}_{k-1})$
6: **end for**
7: **Output:** $\hat{\boldsymbol{v}} \Leftarrow \mathcal{P}_C(\boldsymbol{u} - \gamma(\boldsymbol{\Psi^{-1}})^{\boldsymbol{T}}\boldsymbol{w}_{K_p})$

7.3 Hyperparameter-sensitivity analysis

The reconstruction problem is underdetermined because the DDE compressively maps a high-dimensional spectral-angular object into a spectral-only measurement. Therefore, the fidelity term alone cannot sufficiently constrain the solution space. The regularization terms act as priors that reduce this ill-posedness by favoring physically plausible object distributions.

In our implementation, the spatial regularization weight α controls the strength of the L_1 total-variation prior along the spatial/angular dimension, while the spectral regularization weight β controls the strength of the L_2 total-variation prior along the wavelength dimension. The former favors piecewise-continuous spatial structures, and the latter favors smooth spectral responses. These priors are consistent with many hyperspectral scenes, where objects often contain spatially structured regions and spectra that vary smoothly with wavelength.

To evaluate the sensitivity to these hyperparameters, we sweep α and β over a broad range and calculate the reconstruction MAE. As shown in Fig. S20a, the reconstruction error is high when the regularization is absent or severely imbalanced. However, a broad low-error region exists for intermediate values of α and β, indicating that the reconstruction does not rely on a narrowly tuned hyperparameter pair. Figure S20b shows the ground truth.

Representative reconstructions are shown in Fig. S20c. When α is too small, spatial artifacts remain because the spatial solution space is weakly constrained. When β is too small, the reconstruction shows stronger spectral fluctuations. Conversely, overly large regularization weights suppress valid object variations and cause oversmoothing. These results show that the current reconstruction is robust within a practical parameter range, while also clarifying the limitations of the prior-based approach. For samples with highly random spatial textures, sharp spectral resonances, or rapidly changing dynamics that violate the assumed spatial-spectral priors, reconstruction quality may degrade. In such cases, adaptive regularization or data-driven priors may be required.

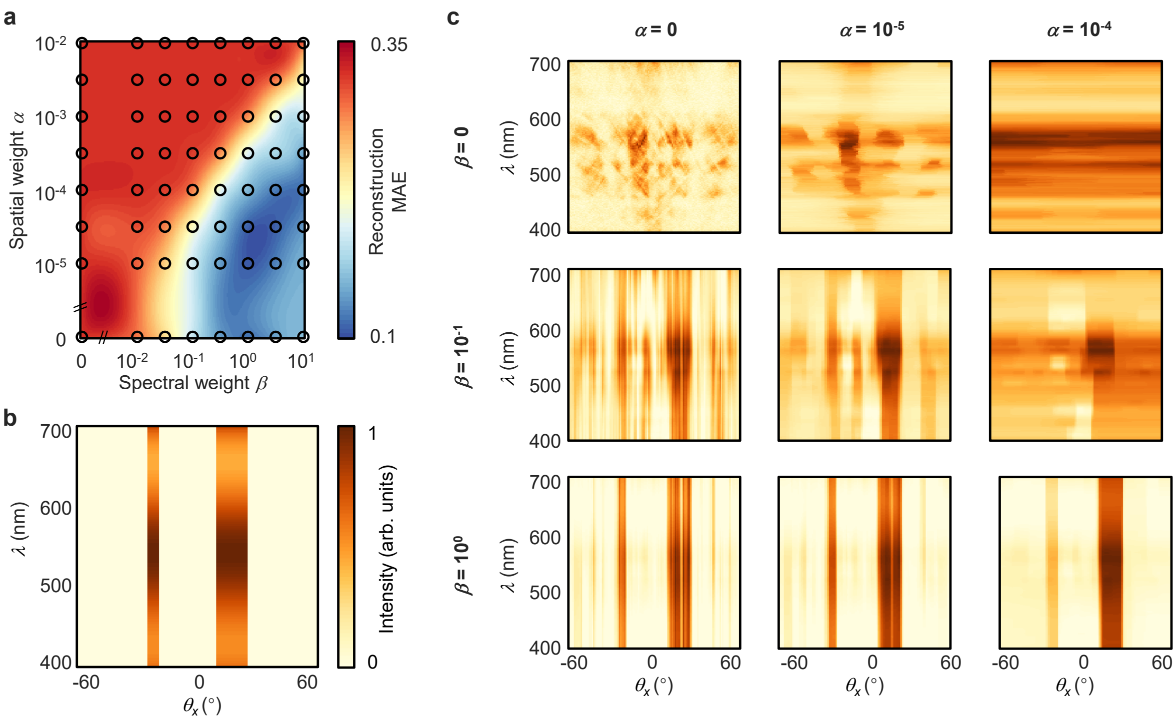

Fig. S20: Hyperparameter-sensitivity analysis of the reconstruction algorithm. a, Reconstruction MAE as a function of the spatial regularization weight α and spectral regularization weight β. The black circles mark the sampled hyperparameter combinations. b, Ground-truth spectral-angular object used for the analysis. c, Representative reconstructions under different combinations of α and β.

7.4 Field of view analysis

We experimentally demonstrate that our method can accurately reconstruct object information over a large field of view (FoV) of $[-60°, 60°]$. In these experiments, a single slit object provided uniform illumination over a 5.5° span, while the central incident angle was swept from $-60°$ to $60°$.

Figures S21a and S21b present reconstruction results for the slit object at different central incident angles, with each color corresponding to a specific angle. The average mean absolute error (MAE) of the reconstructions is 6.27% in the spectral dimension and 6.44% in the angular dimension (Fig. S21c). The MAE is defined as

$$\mathrm{MAE} = \frac{1}{N}\sum_{i=1}^{N}\left|\mathrm{GT}_i - \mathrm{Rec}_i\right|, \tag{S20}$$

where GT_i and Rec_i denote the i-th element of ground truth and reconstructed values respectively, N is the total number of elements. Supplementary Movie 1 further provides an animation of the setup, measurements, and reconstructions, illustrating objects with varying spectral distributions across incident angles from $-60°$ to $60°$. These results confirm the high reconstruction fidelity over the entire FoV.

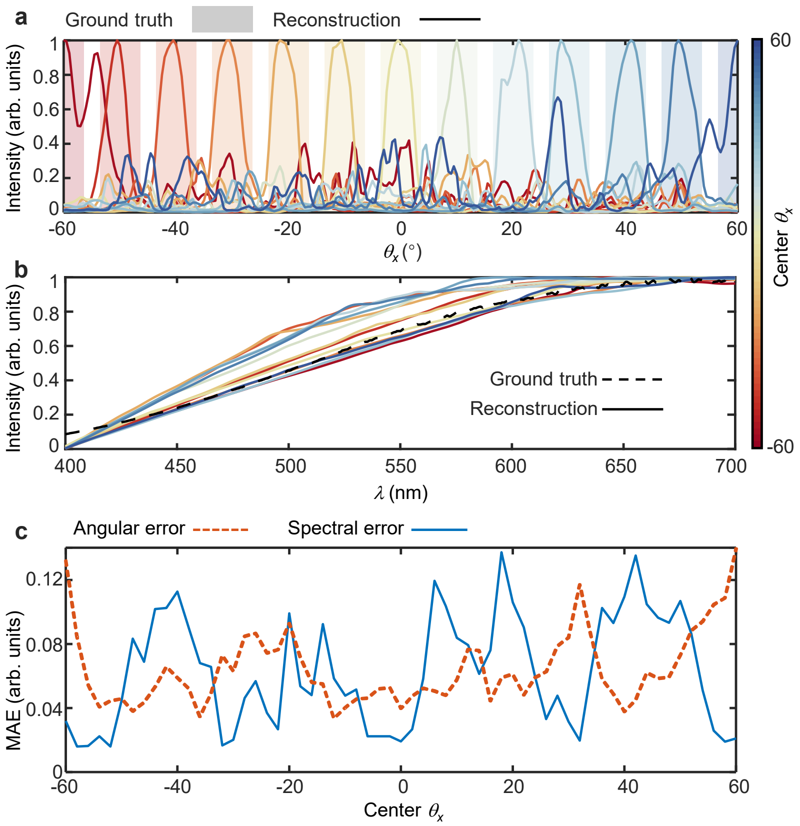

Fig. S21: **Analysis of the imaging field of view. a**, Angular distributions of the reconstructed slit object as its central incident angle moves from $-60°$ to $60°$. **b**, Corresponding spectral distributions. **c**, Mean absolute error of the reconstruction across the FoV of $[-60°, 60°]$.

Importantly, the 120° FoV demonstrated here is not limited by our design but rather a constraint of the experimental setup, which cannot provide illumination at larger angles. As shown by simulations in Fig. S22, our system's transmission matrix remains well-conditioned for encoding over a FoV of $[-90°, 90°]$.

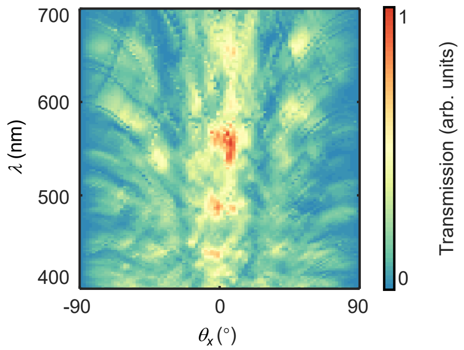

Fig. S22: **Simulated system transmission matrix over a field of view of** $[-90°, 90°]$**.**

7.5 Imaging resolution analysis

To experimentally evaluate the angular resolution of the single-fiber hyperspectral imaging system, we perform a double-slit resolution experiment, as shown in Fig. S23a. Two 2-mm-wide slits separated by a 2-mm gap are placed at a working distance of 40 mm from the DDE. This geometry corresponds to a half-pitch angular resolution of $\Delta\theta \approx \tan^{-1}\left(\frac{2\ \mathrm{mm}}{40\ \mathrm{mm}}\right) \approx 2.9°$. The double-slit target is scanned across the field of view by varying the center angle δ from $-60°$ to $60°$. For each center angle, the spectral measurement is reconstructed independently, as shown in Fig. S23b.

We quantify the resolvability using the dip contrast between the two reconstructed peaks, defined as

$$C_{\mathrm{dip}} = 1 - \frac{I_{\mathrm{dip}}}{\sqrt{I_1 I_2}},$$

where I_1 and I_2 are the intensities of the two reconstructed peaks, and I_{dip} is the minimum intensity between them. A higher dip contrast indicates better separation between the two slits. The results show that the two slits can be resolved over most of the extended field of view, as shown in Fig. S23c. The reconstruction degrades near the field boundary, where incomplete calibration leads to a single-peak reconstruction.

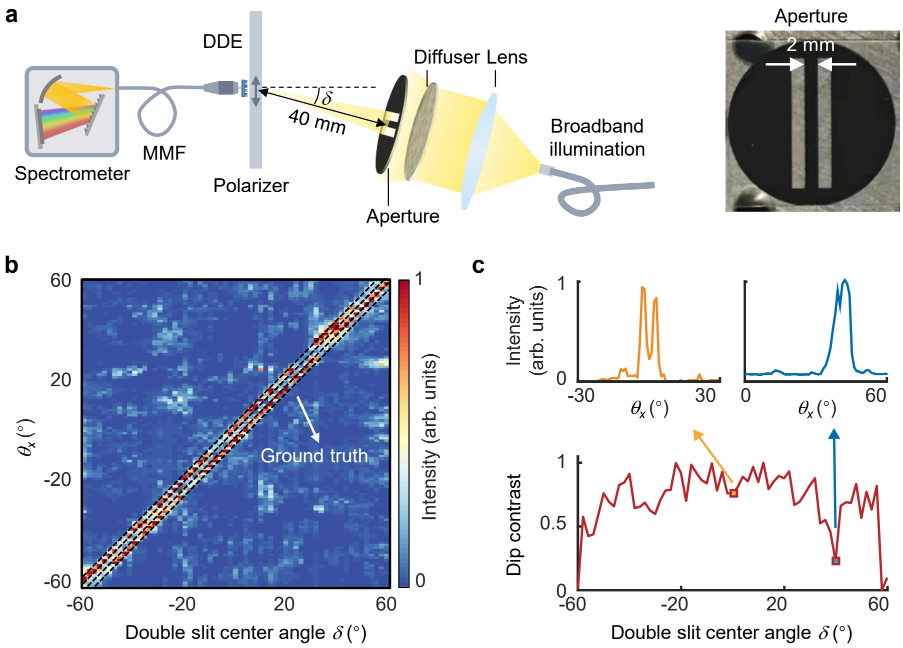

Fig. S23: **Experimental evaluation of angular resolution. a,** Experimental setup for the double-slit resolution test. A double-slit aperture with two 2-mm-wide slits separated by a 2-mm gap is placed 40 mm from the DDE and scanned across the field of view by varying the center angle δ. **b,** Reconstructed angular intensity map as a function of the double-slit center angle δ. The dashed lines indicate the ground-truth angular positions of the two slits. **c,** Representative reconstructed angular profiles and the corresponding dip contrast as a function of δ.

8 Robust hyperspectral imaging under dynamic fiber distortion

Our method demonstrates robustness to fiber distortion. Multimode fibers inherently possess a nearly random transmission matrix due to modal dispersion and coupling, which distorts transmitted images[11,38–40]. The transmission matrix's sensitivity to minor imperfections and external perturbations further complicates practical applications. Although the spatial distribution of the optical field is distorted during propagation through the fiber, the average intensity at each wavelength remains stable. Therefore, our strategy maintains stable performance even when the fiber configuration is distorted.

As shown in Fig. S24a and c, the fiber is bent or twisted by hand, yet the spectral-only measurements remain stable. We recorded 91 frames of measurements under different distorted states, as shown in Fig. S24b, with a mean variance of only 5.42×10^{-5}. Each spectral measurement is reconstructed into the corresponding spectral-angular distribution of the incident light (with the incident light unchanged), as shown in Figs. S24d and S24e. Supplementary Movie 2 provides an animation of this process. The variance of the reconstructed results along the angular and spectral directions is 8.52×10^{-6} and 2.93×10^{-4}, respectively, demonstrating that our method can achieve stable imaging in complex and dynamic environments. This highlights our approach to fiber imaging or communication applications with distorted environments.

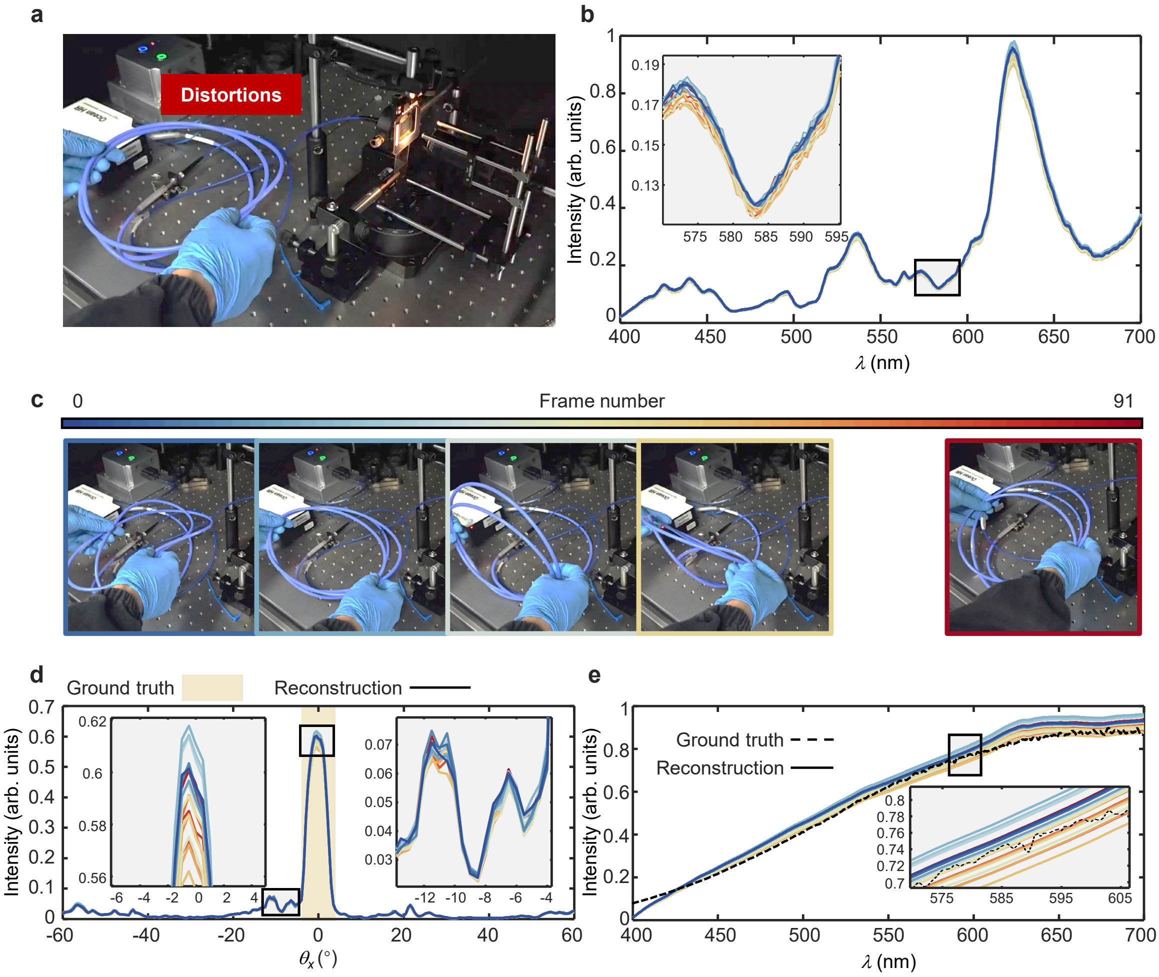

Fig. S24: **Analysis of system robustness to fiber distortion. a**, Experimental setup. Distortions are introduced by manually bending or twisting the fiber. **b**, The measurements exhibit minor changes in relative intensity, while the relative intensity between different wavelengths remains stable. **c**, Different frames of acquisition correspond to distinct fiber distortions. **d**, Reconstructed angular distributions. **e**, Reconstructed spectral distributions.

9 2D hyperspectral imaging experiments

9.1 Experiment setup

The windmill sample shown in Fig. 3f of the main text is custom-built by placing four color filters behind a windmill-shaped opaque aperture. The four transparent triangular regions are covered by yellow, red, green, and blue filters, respectively, thereby producing spatially varying spectral characteristics. For the regional spectral comparison in Fig. 3h, the ground truth spectra are measured separately by recording the transmitted spectrum of the illumination light after passing through each corresponding color filter using a spectrometer.

In addition to this regional spectral reference, we further characterize the full windmill sample using a commercially available line-scan hyperspectral camera (FSIQ, FigSpec). This measurement provides a spatial-spectral reference for the reconstructed wavelength slices.

As shown in Fig. S25, the reconstructed slices reproduce the main spatial distribution and wavelength-dependent filter responses observed in the hyperspectral-camera measurement, providing additional validation beyond the regional spectral comparison in Fig. 3h.

For the biological sample shown in Fig. 4 of the main text, the same stained mouse gastric tumor tissue slice is characterized using the same hyperspectral camera (FSIQ, FigSpec). The ground-truth spectra in Fig. 4e are extracted by averaging the hyperspectral-camera measurements over representative tissue regions corresponding to those used in the single-fiber reconstruction.

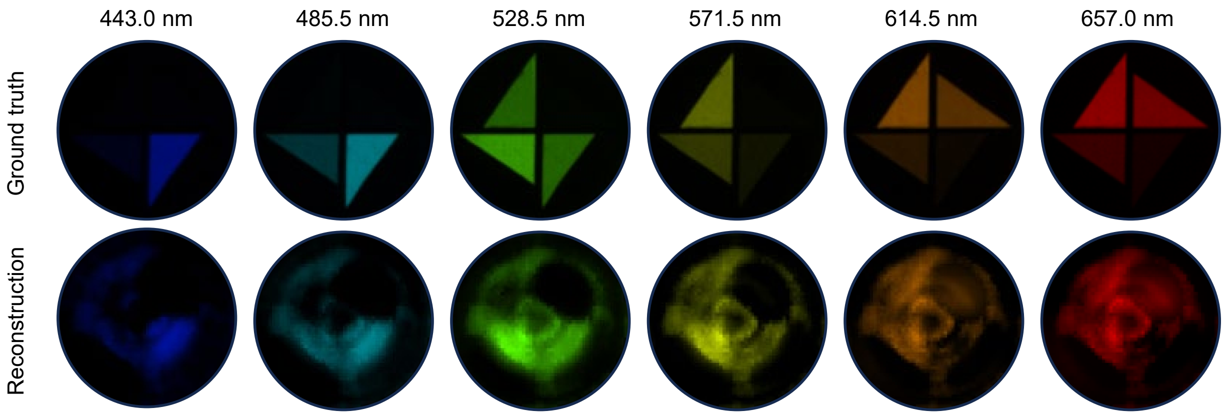

Fig. S25: Spatial-spectral characterization of the windmill sample. The top row shows the hyperspectral-camera ground truth at representative wavelengths, and the bottom row shows the corresponding reconstructed wavelength slices from our system.

To construct 2D hyperspectral samples with a $(\lambda, \theta_x, \theta_y)$ distribution, we illuminate the real-space colored sample with convergent broadband light, as depicted in Fig. S26. By setting the focal point of the convergent illumination at the small aperture of the DDE, the real-space sample $o(\lambda, x, y)$ is transformed into wavevector space $o(\lambda, \theta_x, \theta_y)$. We rotate the object about the z-axis in $10°$ increments, acquiring a total of 36 measurements, which is equivalent to rotating the imaging module's distal end. The reconstruction results shown in Fig. 3f and Fig. 3g exhibit a FoV spanning $[-25°, 25°]$.

It should be noted that the $[-25°, 25°]$ FoV in the 2D imaging is not fundamentally limited by our method, but rather by the numerical aperture of the lens generating the convergent illumination; thus, the sample can only be illuminated within approximately $[-25°, 25°]$. In 1D imaging, a FoV of $[-60°, 60°]$ or larger has been demonstrated, and the same FoV range is in principle applicable to 2D imaging. Moreover, the use of transmission-mode convergent illumination is not a requirement but a means to improve the signal-to-noise ratio. By employing higher-power light sources and more sensitive spectrometers, our method can be adapted for reflection-mode illumination, for example, in surgical endoscopy, industrial endoscopy, and related applications.

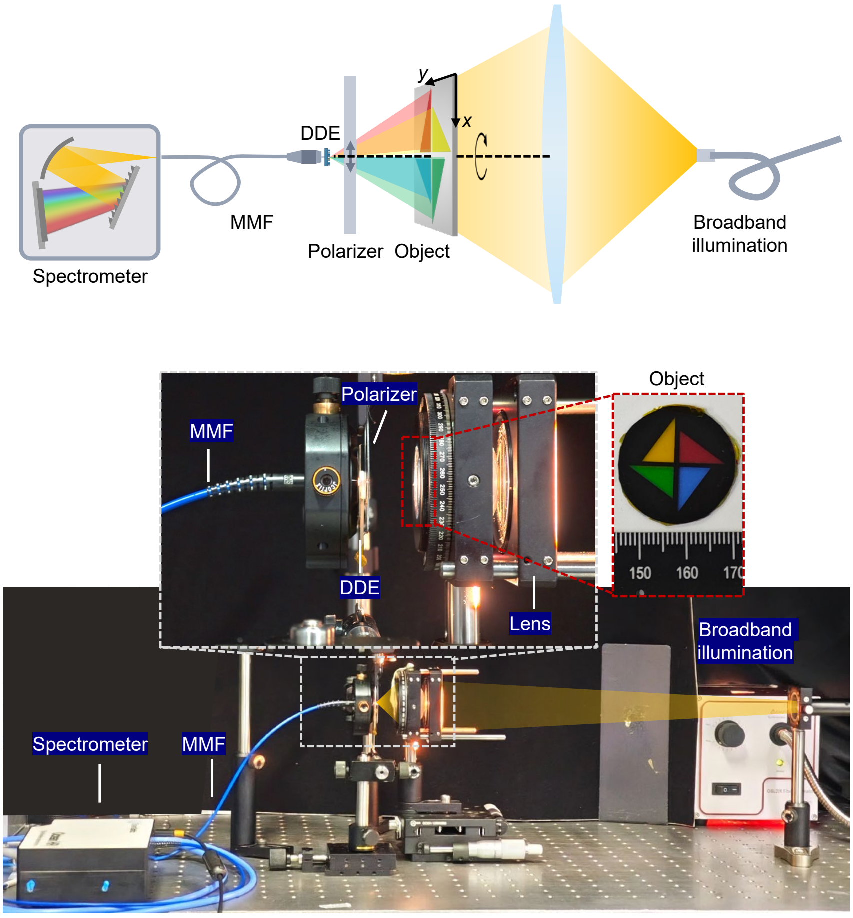

Fig. S26: **Experimental setup for hyperspectral imaging.** Collimated broadband light is focused by a lens to provide convergent illumination. By rotating the object about the z-axis (equivalent to rotating the distal end of the endoscope), we introduce angular diversity in the other spatial direction, thereby enabling hyperspectral imaging.

9.2 Reconstruction algorithm

To extend the 1D reconstruction algorithm to 2D hyperspectral imaging, we first modify the fidelity term to incorporate multiple measurements. The 2D encoding process is expressed as

$$m_i(\lambda) = \iint T_i(\lambda, \theta_x, \theta_y)\, o(\lambda, \theta_x, \theta_y)\, \mathrm{d}\theta_x \mathrm{d}\theta_y. \tag{S21}$$

Here, $T_i(\lambda, \theta_x, \theta_y) = \mathrm{Scan}_i\{T_1(\lambda, \theta_x, \theta_y)\}$, where $\mathrm{Scan}_i\{\cdot\}$ denotes the scanning operation introducing y-diversity, such as rotational or sweep scanning. The variable m_i represents the i-th measurement.

To facilitate computation, the 2D encoding process is vectorized as $\boldsymbol{S}_i\boldsymbol{o} = \boldsymbol{m}_i$. Accordingly, the reconstruction problem can be reformulated as the following optimization:

$$\hat{\boldsymbol{o}} = \underset{\boldsymbol{o}}{\mathrm{argmin}}\, \underbrace{\frac{1}{2}\sum_i \|\boldsymbol{S}_i\boldsymbol{o} - \boldsymbol{m}_i\|_2^2}_{\text{Fidelity term } F(\boldsymbol{o})} + \underbrace{\left\|\boldsymbol{\Psi}^{-1}\boldsymbol{o}\right\|}_{\text{Prior term } R(\boldsymbol{o})}, \tag{S22}$$

This minimization framework is schematically illustrated in Fig. S27. Notably, the optimization problem is solved within the same framework as described in Eqs. S17–S19.

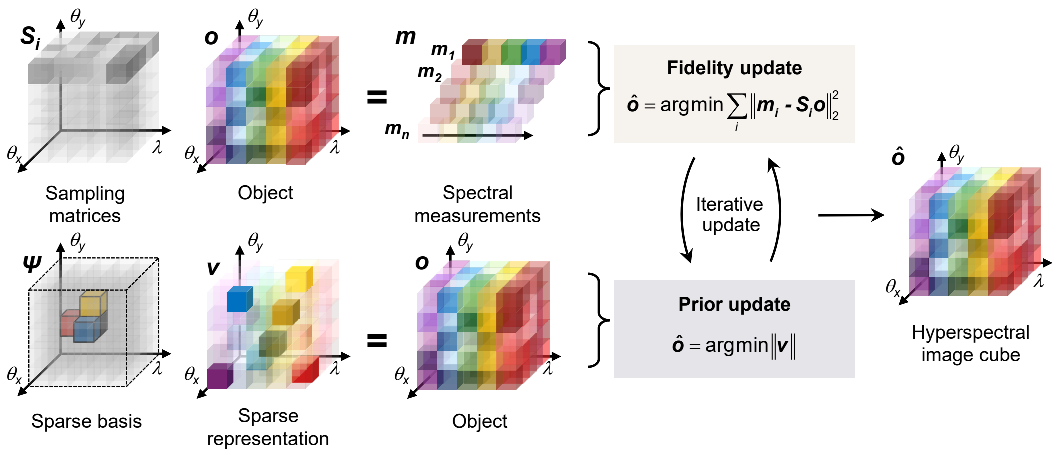

Fig. S27: **Implementation of the 2D hyperspectral reconstruction algorithm.** Our algorithm is implemented by iteratively solving the optimization problem. The optimization problem consists of two terms: the fidelity term, which represents the difference between the current reconstruction and the measurements, and the prior term, which imposes gradient sparsity constraints on the object.

9.3 Imaging depth and angular distribution analysis

The proposed system reconstructs the spectral-angular distribution arriving at the fiber facet. For a point object at (x, y, z), the central incident angles are approximately $\theta_x \approx \tan^{-1}(x/z)$ and $\theta_y \approx \tan^{-1}(y/z)$. Unlike conventional lens-based imaging, the system does not form a sharp intermediate image at a specific object plane, but directly records the incident angular distribution at the fiber facet. Therefore, changing the object depth mainly changes the geometric angle-to-position mapping and introduces a finite angular spread, rather than causing conventional defocus blur. For an aperture diameter D and object distance z, this angular spread scales as $\Delta\theta \sim D/z$.

With a small DDE aperture of 150 µm, a point object at $z = 1$ cm gives $\Delta\theta \sim 0.015$ rad, and the spread further decreases with z. Thus, for millimeter-scale and larger working distances, a point object can be well approximated by a dominant incident angle, giving the angular-encoding system a large effective depth tolerance. However, angular components blocked by sample geometry, surface tilt, self-shadowing, or finite acceptance angle are not measured and therefore cannot be computationally recovered.

10 Scalability to single-mode fibers

Our method does not rely on the spatial modes supported in the optical fibers to transmit information. Therefore, our approach can also be applied with single-mode fibers (SMFs). As shown in Fig. S28, we present our method using an SMF (FCS1-PC/SMA-450-600, JCOPTIX), which has a core diameter of 2.5 microns. We use a supercontinuum laser source (SuperK EVO HP EU-15, NKT Photonics) for higher power illumination to compensate for the low light flux resulting from the small fiber aperture. The light from the laser source passes sequentially through a shortpass filter (FESH0750, Thorlabs) and a polarizing beam-splitter cube (CCM1-PBS251, Thorlabs), illuminating the metagrating. The illumination setup is mounted on a rotating stage to provide different illumination angles.

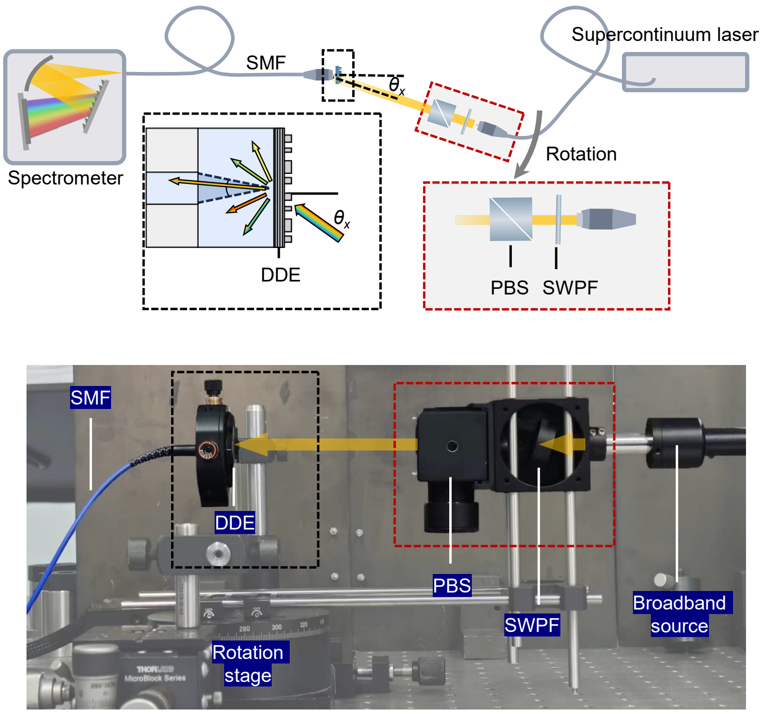

Fig. S28: **Transmission map measurement setups of single-mode fiber system.** SMF, single-mode fiber. PBS, polarizing beam splitter. SWPF, Short wavelength pass filter.

Compared to multimode fibers, SMFs support a narrower spectral transmission band. We selected the wavelength range of 525-700 nm, and the corresponding transmission matrix is shown in Fig. S29a. As expected, the transmission map also exhibits disordered profiles, with distinct and varied spectral and angular slices. Simulations of the reconstructions in Fig. S29b further validate the encoding and decoding capability on hyperspectral images, highlighting the potential applications of our approach in increasing the amount of recoverable information transmitted through highly compact optical waveguides.

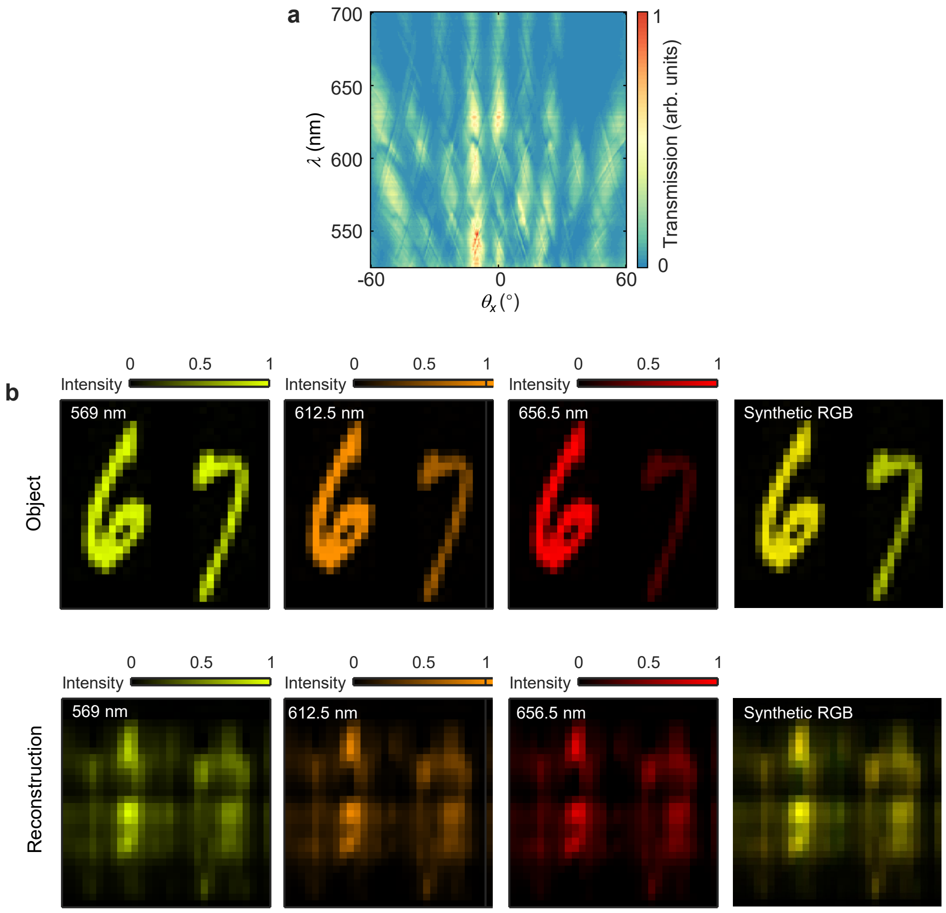

Fig. S29: **Evaluation of the encoding and decoding capability of single-mode fiber system. a**, The transmission map of the single-mode fiber system. **b**, Simulated hyperspectral imaging results of the single-mode fiber system.

11 Light-efficiency and noise-robustness analysis

We first quantify the light efficiency of the system. The DDE encodes information through a wavelength- and angle-dependent transmission, and therefore inevitably redistributes or filters part of the incident light. For s-polarized illumination, the absolute light efficiency is calculated by averaging the system transmission map $T(\lambda, \theta)$ over the calibrated angular range. The wavelength-averaged absolute efficiencies are 3.59% in simulation and 3.8% in experiment.

However, the DDE can also diffract part of the large-angle incident light that would otherwise fall outside the fiber acceptance cone into the collectible angular range. Therefore, we further evaluate the relative light efficiency, defined as the ratio between the collected signals with and without the DDE under the same s-polarized illumination and collection geometry. This metric describes the practical throughput of the DDE-equipped system relative to the

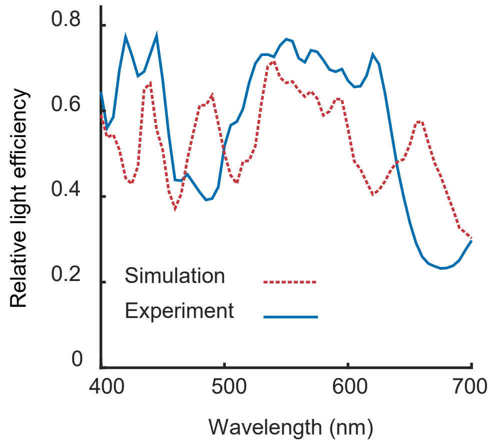

Fig. S30: Relative light efficiency of the DDE-equipped system.

bare fiber-format collection configuration. As shown in Fig. S30, the wavelength-averaged relative efficiencies are 55.8% in simulation and 59.5% in experiment.

In practical applications, the measurement signal-to-noise ratio (SNR) can be limited by the illumination photon budget, encoder efficiency, fiber-coupling efficiency, and spectrometer noise. This limitation may become pronounced when the fiber-core diameter is further reduced. To evaluate the robustness of the proposed compressive encoding and reconstruction scheme under reduced measurement SNR, we perform a numerical noise-robustness analysis.

The simulated object has the spatial pattern of the letter "A", and the same spectral response is assigned to each nonzero spatial position, as shown in Fig. S31a. We first generate clean spectral measurements and then add zero-mean Gaussian noise at specified SNR levels,

$$m_i^{\text{noisy}}(\lambda) = m_i^{\text{clean}}(\lambda) + n_i(\lambda), \tag{S23}$$

where $n_i(\lambda) \sim \mathcal{N}(0, \sigma^2)$. The measurement SNR is defined as

$$\text{SNR} = 20 \log_{10} \left(\frac{\overline{m^{\text{clean}}}}{\sigma} \right), \tag{S24}$$

where $\overline{m^{\text{clean}}}$ denotes the mean intensity of all clean simulated measurements over wavelength and measurement index.

Figure S31b summarizes the mean PSNR and mean SSIM of the reconstructed hyperspectral images under different measurement SNRs. The reconstruction quality remains stable from the noise-free case to 30 dB, and the object can still be reliably reconstructed at 20 dB.

Representative reconstruction results are shown in Fig. S31c. At an SNR of 30 dB, the 4σ noise fluctuation range corresponds to approximately 12.7% of the mean clean signal intensity, and the reconstruction remains close to the noise-free result. At an SNR of 20 dB, the 4σ fluctuation range increases to approximately 40.0% of the mean clean signal intensity. Even under this strongly fluctuating measurement condition, the spectral response and spatial distribution can still be reconstructed. These results demonstrate the robustness of the encoding and decoding scheme to moderate measurement noise, while indicating the importance of improving photon efficiency for smaller-core fibers or illumination-limited conditions.

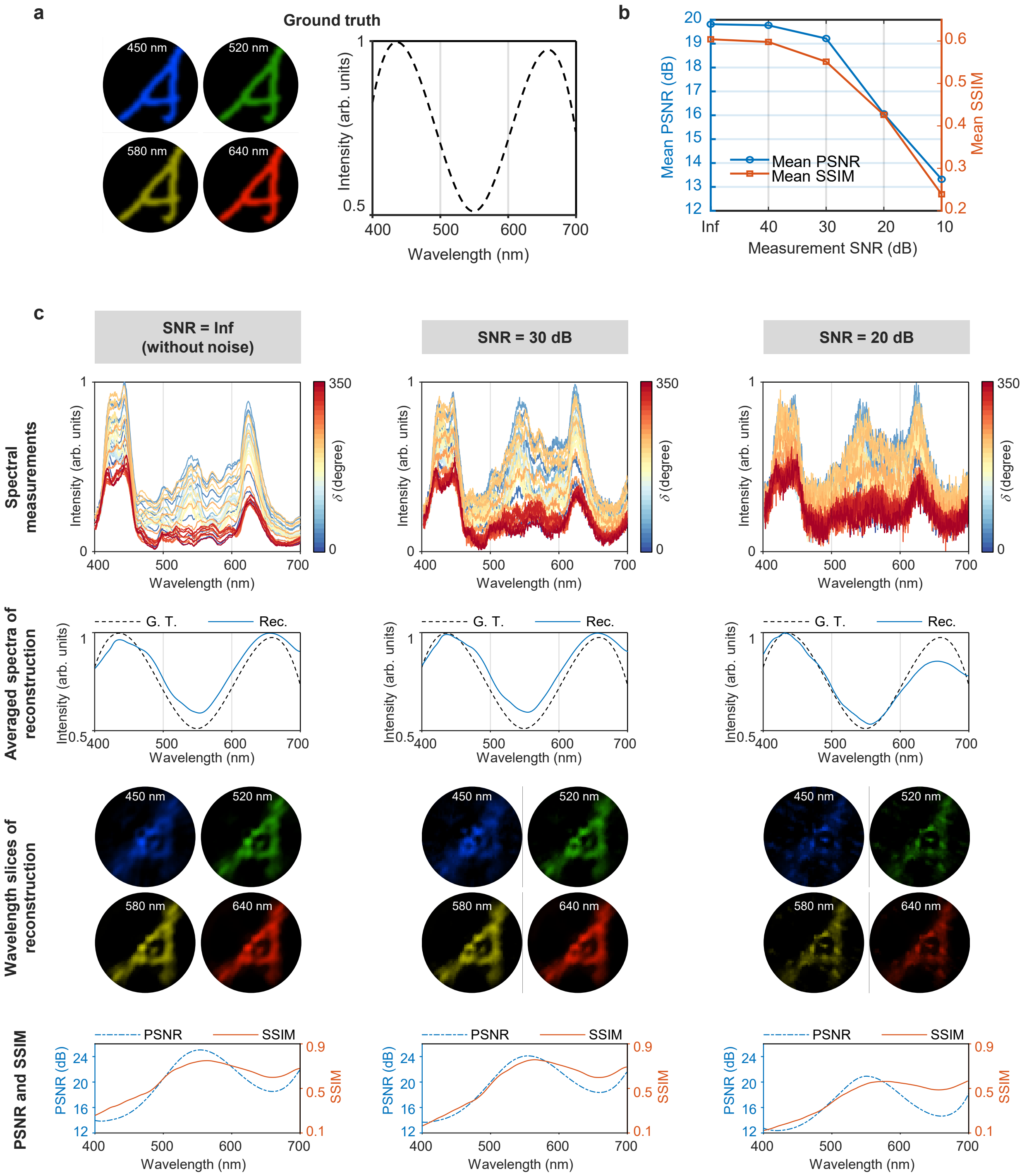

Fig. S31: Noise-robustness analysis of the proposed compressive reconstruction scheme. **a**, Simulated hyperspectral object at representative wavelengths and spectral response assigned to the object. **b**, Mean PSNR and mean SSIM of the reconstructed hyperspectral images under different measurement SNRs. **c**, Representative reconstruction results under different SNR conditions. For each condition, the simulated spectral measurements, averaged reconstructed spectrum, representative wavelength slices, and wavelength-dependent PSNR and SSIM are shown.

12 DDE fabrication

The DDE is fabricated through a commercial service (Nanjing Nanzhi Advanced Opto-electronic Integration Technology Research Institute Co., Ltd.). The process (Methods) is schematically shown in Fig. S32.

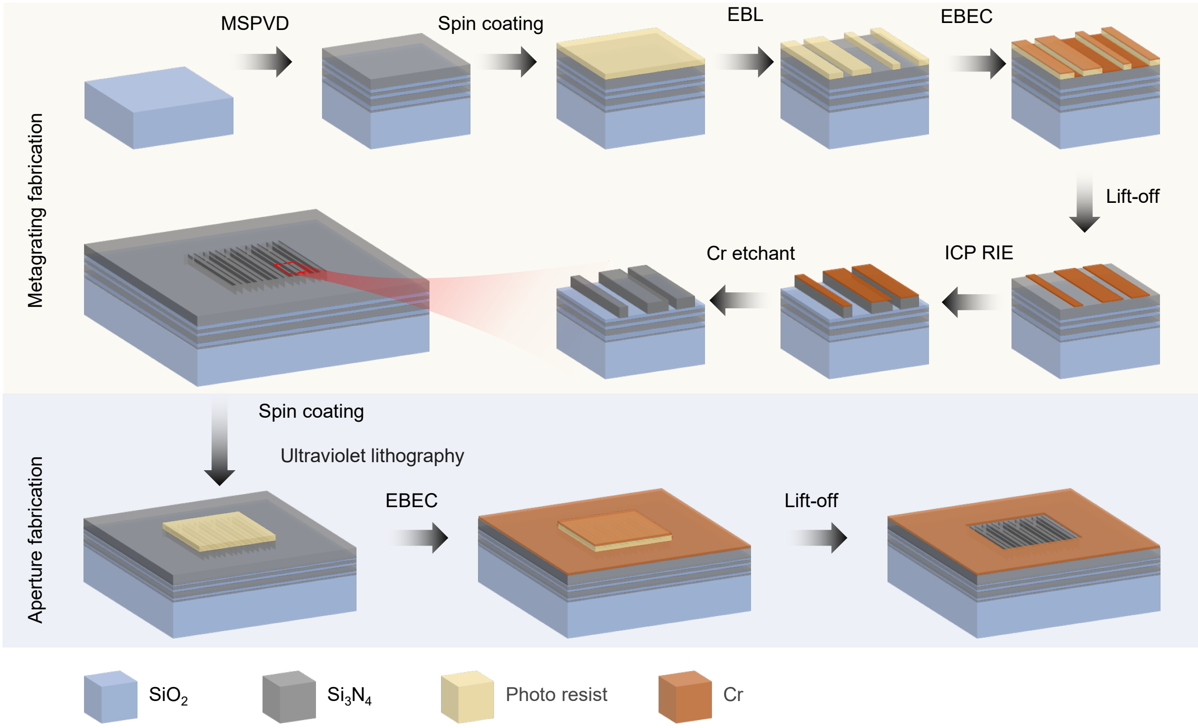

Fig. S32: **Schematic of the fabrication process.** MSPVD: magnetron sputtering physical vapor deposition. EBL: electron beam lithography. EBEC: electron beam evaporation coating. ICP RIE: inductively coupled plasma reactive-ion etching.

Supplementary Movie 1: Spectral-angular reconstruction across a field of view of $[-60°, 60°]$

The video first presents an animated illustration of the system configuration and the reconstruction workflow. Following the experimental setup described in Methods, the slit aperture moves from $-60°$ to $60°$, with a step size of $2°$ driven by a motorized rotational stage, creating incident light with varying incident angles. During this process, different optical filters are installed to generate incident light with diverse spectral distributions, as shown on the left. A total of 61 spectral curves are collected, each of which is individually reconstructed into a spectral-angular distribution, as shown on the right. This demonstration shows that our method effectively reconstructs incident light with different spectra and angular distributions. The spectral measurements are acquired with a 400 ms integration time and an approximately 1 s interval between consecutive spectra. The reconstructions shown in the video are performed offline, with an average reconstruction time of 26.03 s per measurement on a common laptop equipped with an NVIDIA 3060 laptop GPU and an Intel i9-12900H CPU.

Supplementary Movie 2: Robust spectral signal transmission through a single multimode fiber and spectral-angular reconstruction

The video first presents an animated illustration of the system configuration and the reconstruction workflow. The imaging system is set to continuous acquisition mode, and fiber distortions, such as bending and twisting, are manually introduced, as shown on the left. The spectral measurements, shown on the right, remain robust to distortion, with only minor changes in relative intensity. Thanks to this characteristic, the spectral-angular distribution can be robustly reconstructed even under fiber distortions. The data acquisition and offline reconstruction settings are the same as those described for Supplementary Movie 1.

References

[1] Tsvirkun, V. *et al.* Flexible lensless endoscope with a conformationally invariant multi-core fiber. *Optica* **6**, 1185–1189 (2019).

[2] Sun, J. *et al.* Quantitative phase imaging through an ultra-thin lensless fiber endoscope. *Light: Science & Applications* **11**, 204 (2022).

[3] Badt, N. & Katz, O. Real-time holographic lensless micro-endoscopy through flexible fibers via fiber bundle distal holography. *Nature Communications* **13**, 6055 (2022).

[4] Fröch, J. E. *et al.* Real time full-color imaging in a meta-optical fiber endoscope. *eLight* **3**, 13 (2023).

[5] Song, P. *et al.* Ptycho-endoscopy on a lensless ultrathin fiber bundle tip. *Light: Science & Applications* **13**, 168 (2024).

[6] Skarsoulis, K., Makris, K., Moser, C. & Psaltis, D. Ptychographic imaging with a fiber endoscope via wavelength scanning. *Optica* **11**, 782–790 (2024).

[7] Lich, J., Glosemeyer, T., Czarske, J. & Kuschmierz, R. Single-shot 3d incoherent imaging with diffuser endoscopy. *Light: Advanced Manufacturing* **5**, 1–11 (2024).

[8] Choi, Y. *et al.* Scanner-free and wide-field endoscopic imaging by using a single multimode optical fiber. *Physical Review Letters* **109**, 203901 (2012).

[9] Čižmár, T. & Dholakia, K. Exploiting multimode waveguides for pure fibre-based imaging. *Nature Communications* **3**, 1027 (2012).

[10] Leite, I. T. *et al.* Three-dimensional holographic optical manipulation through a high-numerical-aperture soft-glass multimode fibre. *Nature Photonics* **12**, 33–39 (2018).

[11] Plöschner, M., Tyc, T. & Čižmár, T. Seeing through chaos in multimode fibres. *Nature Photonics* **9**, 529–535 (2015).

[12] Li, S., Horsley, S. A., Tyc, T., Čižmár, T. & Phillips, D. B. Memory effect assisted imaging through multimode optical fibres. *Nature Communications* **12**, 3751 (2021).

[13] Stellinga, D. *et al.* Time-of-flight 3d imaging through multimode optical fibers. *Science* **374**, 1395–1399 (2021).

[14] Wen, Z. *et al.* Single multimode fibre for in vivo light-field-encoded endoscopic imaging. *Nature Photonics* **17**, 679–687 (2023).

[15] Tearney, G., Shishkov, M. & Bouma, B. Spectrally encoded miniature endoscopy. *Optics Letters* **27**, 412–414 (2002).

[16] Yelin, D. *et al.* Three-dimensional miniature endoscopy. *Nature* **443**, 765–765 (2006).

[17] Barankov, R. & Mertz, J. High-throughput imaging of self-luminous objects through a single optical fibre. *Nature Communications* **5**, 5581 (2014).

[18] Kolenderska, S. M., Katz, O., Fink, M. & Gigan, S. Scanning-free imaging through a single fiber by random spatio-spectral encoding. *Optics Letters* **40**, 534–537 (2015).

[19] Xie, N., Tanguy, Q. A., Froch, J. E., Bohringer, K. F. & Majumdar, A. Spectrally encoded nonscanning imaging through a fiber. *ACS Photonics* **11**, 1117–1124 (2024).

[20] Green, R. O. *et al.* Imaging spectroscopy and the airborne visible/infrared imaging spectrometer (AVIRIS). *Remote Sensing of Environment* **65**, 227–248 (1998).

[21] Bao, F. *et al.* Heat-assisted detection and ranging. *Nature* **619**, 743–748 (2023).

[22] Gehm, M. E., John, R., Brady, D. J., Willett, R. M. & Schulz, T. J. Single-shot compressive spectral imaging with a dual-disperser architecture. *Optics Express* **15**, 14013–14027 (2007).

[23] Wagadarikar, A., John, R., Willett, R. & Brady, D. Single disperser design for coded aperture snapshot spectral imaging. *Applied Optics* **47**, B44–B51 (2008).

[24] Cao, X. *et al.* Computational snapshot multispectral cameras: Toward dynamic capture of the spectral world. *IEEE Signal Processing Magazine* **33**, 95–108 (2016).

[25] Yuan, X., Brady, D. J. & Katsaggelos, A. K. Snapshot compressive imaging: Theory, algorithms, and applications. *IEEE Signal Processing Magazine* **38**, 65–88 (2021).

[26] Wang, Z. *et al.* Single-shot on-chip spectral sensors based on photonic crystal slabs. *Nature Communications* **10**, 1020 (2019).

[27] Xiong, J. *et al.* Dynamic brain spectrum acquired by a real-time ultraspectral imaging chip with reconfigurable metasurfaces. *Optica* **9**, 461–468 (2022).

[28] Zhang, W. *et al.* Handheld snapshot multi-spectral camera at tens-of-megapixel resolution. *Nature Communications* **14**, 5043 (2023).

[29] Yako, M. *et al.* Video-rate hyperspectral camera based on a cmos-compatible random array of fabry–pérot filters. *Nature Photonics* **17**, 218–223 (2023).

[30] Bian, L. *et al.* A broadband hyperspectral image sensor with high spatio-temporal resolution. *Nature* **635**, 73–81 (2024).

[31] Hugonin, J. P. & Lalanne, P. Reticolo software for grating analysis. *arXiv preprint arXiv:2101.00901* (2021).

[32] Byrnes, S. J. Multilayer optical calculations. *arXiv preprint arXiv:1603.02720* (2016).

[33] Luce, A., Mahdavi, A., Marquardt, F. & Wankerl, H. TMM-Fast, a transfer matrix computation package for multilayer thin-film optimization: tutorial. *JOSA A* **39**, 1007–1013 (2022).

[34] Yasuma, F., Mitsunaga, T., Iso, D. & Nayar, S. K. Generalized assorted pixel camera: postcapture control of resolution, dynamic range, and spectrum. *IEEE transactions on image processing* **19**, 2241–2253 (2010).

[35] Deng, L. The mnist database of handwritten digit images for machine learning research [best of the web]. *IEEE signal processing magazine* **29**, 141–142 (2012).

[36] Beck, A. & Teboulle, M. A fast iterative shrinkage-thresholding algorithm for linear inverse problems. *SIAM Journal on Imaging Sciences* **2**, 183–202 (2009).

[37] Beck, A. & Teboulle, M. Fast gradient-based algorithms for constrained total variation image denoising and deblurring problems. *IEEE Transactions on Image Processing* **18**, 2419–2434 (2009).

[38] Cao, H., Mosk, A. P. & Rotter, S. Shaping the propagation of light in complex media. *Nature Physics* **18**, 994–1007 (2022).

[39] Bertolotti, J. & Katz, O. Imaging in complex media. *Nature Physics* **18**, 1008–1017 (2022).

[40] Gigan, S. Imaging and computing with disorder. *Nature Physics* **18**, 980–985 (2022).